

**NOAA NESDIS  
CENTER for SATELLITE APPLICATIONS and  
RESEARCH**

**Algorithm Theoretical Basis Document  
For  
Daytime Cloud Optical and Microphysical  
Properties (DCOMP)**

*Andi Walther UW/CIMSS  
Andrew K. Heidinger, NOAA/NESDIS/STAR*

Version 1.1

10 July 2017

## TABLE OF CONTENTS

1	INTRODUCTION.....	9
1.1	Purpose of This Document.....	9
1.2	Who Should Use This Document.....	9
1.3	Inside Each Section.....	9
1.4	Products Generated.....	10
1.5	Observing system overview.....	11
1.5.1	Characteristics of instruments used.....	11
2	ALGORITHM DESCRIPTION.....	12
2.1	Processing Outline.....	14
2.2	Algorithm Input.....	20
2.2.1	Control parameters.....	20
2.2.2	Primary Sensor Data.....	20
2.2.3	Ancillary Data.....	21
2.2.4	Pre-derived Data.....	22
2.2.5	Look-up-tables.....	23
2.3	Theoretical Description.....	23
2.3.1	Physics of the Problem.....	23
2.3.1.1	Basic Considerations.....	24
2.3.1.2	Radiative Transfer Calculations.....	26
2.3.1.3	Impact of Surface Reflection.....	31
2.3.1.4	Forward model in near-infrared channel around 3.75 micron.....	31
2.3.2	Mathematical Description.....	32
2.3.2.1	Structure and Interpolation of LUT Data.....	33
2.3.2.1.1.1	Structure of LUTs.....	33
2.3.2.1.1.2	Interpolation.....	33
2.3.2.1.1.3	Compute Partial Derivatives.....	36
2.3.2.2	Atmospheric Correction.....	37
2.3.2.2.1	Atmospheric Correction for Rayleigh scattering.....	39
2.3.2.2.2	Atmospheric Correction for Aerosol Scattering Effects.....	42
2.3.2.2.3	Atmospheric Corrections for Water Vapor Absorption and Trace Gases	43
2.3.2.2.4	Ozone.....	44
2.3.2.3	Optimal Estimation Inversion Technique.....	45
2.3.2.4	Estimation of Prior Values and their Uncertainty.....	47
2.3.2.5	Estimation of Forward Model Uncertainty.....	48
2.4	Algorithm Product Output.....	49
2.4.1	Output.....	49
2.4.2	Quality Flags.....	50
2.4.3	Processing Information Flag.....	50
2.4.4	Metadata.....	51
2.5	Performance Estimates.....	51
2.5.1	Test Data Sets and Output.....	51
2.5.1.1	Example for geostationary sensor: SEVIRI.....	51
2.5.1.2	Example for polar-orbiting data: VIIRS/NPP Suomi.....	53
2.5.1.3	DCOMP and the PATMOS-x AVHRR climate data set.....	53
2.5.2	Sensor Effects.....	55
2.6	Practical considerations.....	55

2.6.1	Numerical Computation Considerations .....	55
2.6.2	Programming and Procedural Considerations.....	55
2.6.3	Quality Assessment and Diagnostics .....	56
2.6.4	Exception Handling.....	56
2.7	Algorithm Validation .....	56
2.7.1	Inter-comparison with Products of Other Research Groups .....	57
2.7.2	Comparison with MODIS, AMSR-E along a CloudSat Track .....	60
2.7.3	Long-period MODIS Analysis .....	61
2.7.3.1	Comparison of Cloud Optical Depth.....	61
2.7.3.2	Comparison of Cloud Particle Size .....	62
2.7.3.3	Comparison of Cloud Optical Depth Ice phase.....	63
2.7.4	Comparison of DCOMP/LWP with AMSR-E .....	63
2.7.5	Error Budget.....	64
3	ASSUMPTIONS AND LIMITATIONS.....	65
3.1	Performance .....	65
3.2	Assumed Sensor Performance.....	65
3.3	Pre-Planned Product Improvements.....	66
4	REFERENCES .....	66

## LIST OF FIGURES

Figure 1 Channel response functions for DCOMP channels 1-5 for five sensors.....	11
Figure 2 High-level flowchart of the DCOMP algorithm.....	17
Figure 3 DCOMP: Pixel-based flow chart.....	18
Figure 4 Flow chart of 1D-Var inversion retrieval loop. ....	19
Figure 5 Comparison of Heymsfield method to a traditional method (dashed line) of calculating the ice water path from optical depth. ....	26
Figure 6 Example of simulated cloud reflectances as a function of optical depth and effective radius for DCOMP channel 1 (ABI-channel 2; left) and DCOMP channel 3 ( channel 5; right). Satellite zenith is 20, Local zenith angle = 20 and Relative azimuth angle = 140.....	28
Figure 7 Theoretically computed cloud reflectance function for water phase of GOES- ABI channels 2 and 6 (DCOMP channel 1 and 3) for an arbitrary geometrical observation constellation. ....	29
Figure 8 Same as Figure 6 , but for ice clouds.....	29
Figure 9 Pictorial depiction of LUT linear interpolation in both one and two dimensions. .....	36
Figure 10 Potential error in percent if Rayleigh correction is not applied as a function of $\tau_c$ and solar zenith angle. Observation angle is 43 degrees and effective radius is $8 \mu m$ .....	40
Figure 11 Water vapor transmission as a function of absorber amount. ....	44
Figure 12 Ozone transmission as a function of absorber amount.....	45
Figure 13 Full disk true color image from SEVIRI 13UTC on 1 August 2006.....	52
Figure 14 Results of the retrieval for 1 August 2006 13:00UTC for SEVIRI. Upper panel shows optical depth (left) and effective radius (right). Lower panel shows liquid water path (left) and ice water path (right). ....	53
Figure 15 True color image for VIIRS/NPP scene. ....	53
Figure 16 DCOMP output COD (left) and CPS (right) for VIIRS/NPP .....	53
Figure 17 DCOMP Cloud Optical Thickness for one day of PATMOS-x level2b data from NOAA-18.....	54
Figure 18 Comparison of level2b data from the AVHRR PATMOS-x data set ( left) and a similar level-2b data set derived by GOES-EAST satellite .....	54
Figure 19 Time series of Liquid water path from DCOMP results in PATMOS-x data set in comparison to GOES-West results. ....	55
Figure 20 Comparison of DCOMP-COD for liquid water clouds algorithm (AWG) to six other groups. ....	57
Figure 21 Comparison of DCOMP-COD Ice phase with six other groups. ....	58
Figure 22 Comparison of DCOPM-REF all phases with six other groups.....	59

Figure 23 Integrative comparison of ABI products. Upper panel shows CloudSat radar reflectivities with ABI cloud height (white crosses). Second panel shows comparison of DCOMP cloud optical depth of ice (red) and liquid water (green) with MODIS. Third panel shows same, but for effective radius. Bottom panel illustrates comparison of DCOMP liquid water path with AMSR-E. .... 60

Figure 24 Comparison of Cloud Optical thickness for Days 230-239 in 2006 derived from MODIS (MYD06 and MOD06) products and from DCOMP algorithm. Left image shows results for water phase, right image for ice phase. Accuracy and precision of the comparison are shown in the figures. Specs ranges are added as white lines in the figures. .... 62

Figure 25 Comparison of Cloud Particle Size for Days 230-239 in 2006 derived from MODIS (MYD06 and MOD06) products and from DCOMP algorithm. Left image shows results for water phase, right image for ice phase. Accuracy and precision of the comparison are shown in the figures. Specs ranges are added as white lines in the figures. .... 62

Figure 26 Comparison of Water Path for Days 230-239 in 2006 derived from MODIS (MYD06 and MOD06) products and from DCOMP algorithm. Left image shows results for water phase (LWP), right image for ice phase (IWP). Accuracy and precision of the comparison are shown in the figures. Specs ranges are added as white lines in the figures. .... 63

Figure 27 Comparison of AWG-DCOMP Liquid water product to AMSR-E for a two-day period (24-25 August 2006) as a 2D histogram. .... 64

## LIST OF TABLES

Table 1 DCOMP product requirements .....	10
Table 2 Available sensors with channel settings for DCOMP. Available channels are colored with native channel number. Green channels are suggested default choice for each sensor. Yellow channels are available for additional mode or as back-up solutions. ....	12
Table 3 DCOMP primary sensor input .....	20
Table 4 Ancillary input data .....	21
Table 6 DCOMP input: Derived cloud products. ....	22
Table 7 LUT ancillary data .....	23
Table 8 Parameters and mathematical symbols used in Chapter 3.4.1 .....	23
Table 9 Parameters used in the section “Atmospheric Correction” .....	37
Table 10 Global settings for aerosol parameters.....	42
Table 11 Water vapor correction coefficients exemplarily for GOES-ABI.....	43
Table 12 Water vapor correction coefficients for SEVIRI .....	44
Table 13 The error estimated in forward model uncertainty in DCOMP .....	49
Table 14 Algorithm output.....	49
Table 15 Quality Flags in DCOMP output .....	50
Table 16 Processing Information Flags in DCOMP .....	50
Table 18 Validation results of DCOMP.....	64

## LIST OF ACRONYMS

ABI - Advanced Baseline Imager  
AIT - Algorithm Integration Team  
ATBD - algorithm theoretical basis document  
A-Train – Afternoon Train (Aqua, CALIPSO, CloudSat, etc.)  
AVHRR - Advanced Very High Resolution Radiometer  
AWG - Algorithm Working Group  
CALIPSO - Cloud-Aerosol Lidar and Infrared Pathfinder Satellite  
CIMSS - Cooperative Institute for Meteorological Satellite Studies  
CLAVR-x = Cloud Algorithm Retrieval-extended  
DCOMP – Daytime Cloud Optical Microphysical Properties Algorithm  
EUMETSAT- European Organization for the Exploitation of Meteorological Satellites  
F&PS - Function and Performance Specification  
GEOCAT-  
GFS - Global Forecast System  
GOES - Geostationary Operational Environmental Satellite  
MODIS - Moderate Resolution Imaging Spectroradiometer  
MSG - METEOSAT Second Generation  
NASA - National Aeronautics and Space Administration  
NCOMP - Nighttime Cloud Optical Microphysical Properties Algorithm  
NOAA - National Oceanic and Atmospheric Administration  
NWP - Numerical Weather Prediction  
OE – Optimal Estimation  
RTM - Radiative transfer model  
SEVIRI - Spinning Enhanced Visible and Infrared Imager  
SSEC – Space Science and Engineering Center  
STAR - Center for Satellite Applications and Research  
UW – University of Wisconsin-Madison  
VIS – Visible Range of Spectrum

## ABSTRACT

This document describes a satellite-based algorithm, which retrieves cloud properties from space: The Daytime Cloud and Optical and Microphysical Properties (DCOMP) algorithm. The retrieved properties are Cloud Optical Depth (COD), Cloud effective Particle size (CPS), Liquid and Ice water path (LWP and IWP).

DCOMP works on all sensors those have observations in a visible channel and in at least one near infrared channel. DCOMP successfully produces results for the geo satellites SEVIRI, GOES series, MTSAT and HIMAWARI and polar-orbiting satellites NOAA-AVHRR series, MODIS, VIIRS/NPP.

Daytime is hereby defined as observations with a solar zenith angle of 65 degrees or below.

COD and CPS are retrieved simultaneously from observations in one visible and one near-infrared channel. The main information content for COD lies in the conservative-scattering channel at about 0.6 micrometer. The absorption channel at 2.2 micrometer provides additional information on CPS and helps indirectly to estimate COD by adjusting the differences in the phase function due to particle size. Liquid and ice water path are calculated subsequently from COD and CPS.

The document first introduces and discusses the physical basics. The document then explains in detail the mathematical methods of all parts of the algorithm including atmospheric correction, inversion method and post-processing.

We show exemplary results of a SEVIRI proxy data set. The results were validated with data from MODIS and other A-TRAIN sensors.

# 1 INTRODUCTION

## 1.1 Purpose of This Document

This algorithm theoretical basis document (ATBD) for Daytime Cloud Optical and Microphysical Properties (DCOMP) provides a high-level description of the physical basis for inferring cloud optical depth (COD), cloud particle size (CPS), liquid water path (LWP) and ice water path (IWP) from imagery taken by sensors which make observations in visible and near-IR spectrum. The COD and CPS will be inferred for all pixels identified as containing cloud by a preprocessed cloud mask. We distinguish clouds as either ice phase or water phase. The latter also include in our definition super-cooled and mixed phase clouds. The COD and CPS are used subsequently to calculate liquid/ice water path (LWP/IWP), whose values can be compared with those, derived from active measurements from space-born instruments such as the Cloud Profiling Radar (CPR) on CloudSat and passive microwave sensors such as AMSR-E or SSM/I, as well as ground-based microwave profilers.

## 1.2 Who Should Use This Document

The intended users of this document are those interested in understanding the physical basis of the algorithms and how to use the output of this algorithm to study or assimilate cloud properties. This document also provides information useful to anyone maintaining or modifying the original algorithm.

## 1.3 Inside Each Section

This document is broken down into the following main sections:

- **Observing System Overview:** Provides relevant details of the needed sensor system and provides a brief description of the products generated by the algorithm.
- **Algorithm Description:** Provides a detailed description of the algorithm including its physical basis, its input, and its output.
- **Test Datasets and Outputs:** Describes test datasets including proxy data from SEVIRI. It also shows output in the form of images.
- **Practical Considerations:** Describes all issues involving numerical computation, programming and procedures, quality assessment and diagnostics and exception handling at a level of detail appropriate for the current algorithm maturity.
- **Assumptions and Limitations:** Provides an overview of the current limitations of the approach and provides the plan for overcoming these limitations with further algorithm development.

## 1.4 Products Generated

The DCOMP algorithm is responsible for generating the DCOMP products, which are cloud optical depth (COD) and cloud particle size (CPS) for all daytime ABI pixels that are detected as cloudy. Subsequently liquid water path (LWP) and ice water path (IWP) products will be derived from COD and CPS.

COD represents the vertical optical thickness between the top and bottom of an atmospheric column. COD is almost independent of wavelength in the visible range of the spectrum. COD has no unit. CPS is supposed to represent the cloud droplet distribution. The cloud effective radius, defined, as the ratio of the third to the second moment of a droplet size distribution, is well suited to fulfill this task. CPS has the unit micrometer ( $\mu\text{m}$ ).

LWP and IWP are a measure of the total mass of water in a cloud column. The unit is gram per square meter ( $\text{g}/\text{m}^2$ ).

In our context, “daytime” is defined to be where the solar zenith angle for a given pixel is less than or equal to 65 degrees, for which DCOMP provides full quality products. To fill a temporal gap between DCOMP and the nighttime cloud properties algorithm (NCOMP) degraded products for solar zenith angles between 65 and 82 degrees will be provided by DCOMP.

The current cloud mask design has four categories: clear, probably clear, probably cloudy and cloudy. The DCOMP products will be derived for pixels that are probably cloudy or cloudy.

**Table 1 DCOMP product requirements**

Requirements				
Product	Range	Accuracy	Precision	
COD	0.5-50	2 or 20% (liquid) 3 or 30% (ice)	2 or 20% (liquid) 3 or 30% (ice)	> 65 degree solar zenith
CPS	0-50 $\mu\text{m}$	4 $\mu\text{m}$ /10 $\mu\text{m}$ (liquid/ice)	4 $\mu\text{m}$ /10 $\mu\text{m}$	> 65 degree solar zenith
LWP		50g/m <sup>2</sup>	30%	> 65 degree solar zenith
IWP		100g/m <sup>2</sup>	40%	> 65 degree solar zenith

## 1.5 Observing system overview

This section gives an overview of the algorithm, including the objectives, characteristics of the instrument and the products generated by the ABI Daytime Cloud Optical and Microphysical Properties algorithm (DCOMP).

### 1.5.1 Characteristics of instruments used

DCOMP runs on several current sensors, which have partly different channel settings and response functions. We will focus exemplarily in this description on four sensors: Imager on GOES-14, ABI on (future) GOES-R, MODIS on AQUA and VIIRS on NPP and AVHRR on NOAA-19.

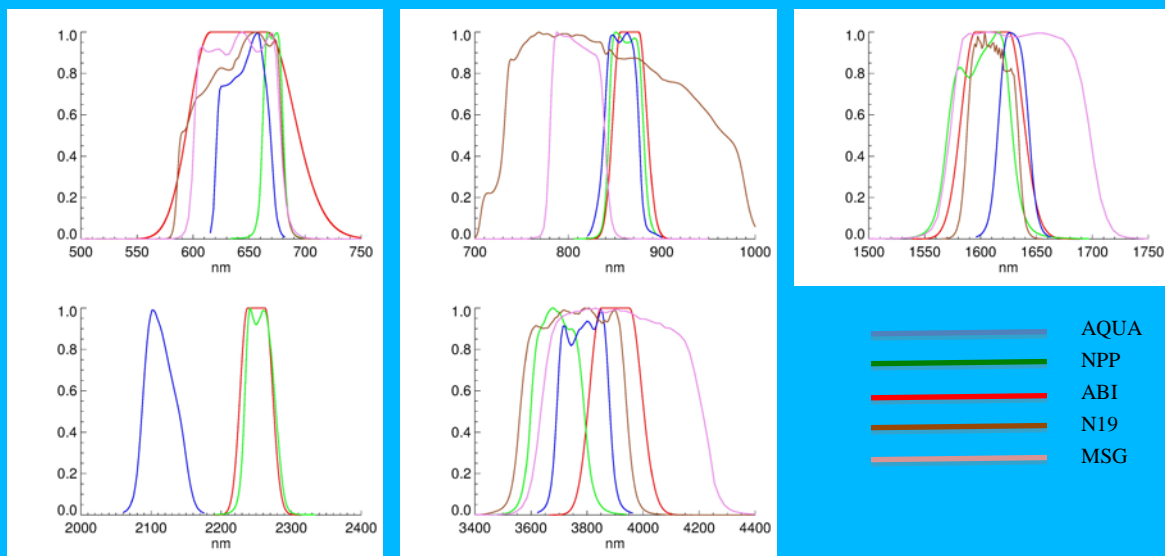


Figure 1 Channel response functions for DCOMP channels 1-5 for five sensors.

Figure 1 shows the spectral response functions in the visible and near-infrared part of the spectra. The differences in spectral response are considered in the LUT generation explained in section below. Table 1 summarizes the channel settings used by the DCOMP approach for all relevant current sensors. DCOMP channel 2 (yellow) is supposed to be back-up channel and also reserved for advanced developments.

**Table 2 Available sensors with channel settings for DCOMP. Available channels are colored with native channel number. Green channels are suggested default choice for each sensor. Yellow channels are available for additional mode or as back-up solutions.**

			Temporal	Spatial	1	2	3	4	5
Sensor	Platform				0.6	0.8	1.6	2.2	3.7
VIIRS NPP	NPP	P	1:30 PM	750 m	M5	M8	M10	M11	M12
MODIS	AQUA	P		1km/4km	1	2	6	7	20
	TERRA	P		1km/4km	1	2	6	7	20
SEVIRI	MSG- 8-10	G	15 min	4km	1	2	3		4
AVHRR	NOAA-series	P	about 2 pm	4 km	1	2	3a		3b
	METOP	P			1	2	3a		3b
GOES Imager	GOES-series	G			1				2
ABI	GOES-R	G			2	3	5	6	7
AHI	HIMAWARI	G			3	4	5	6	7
MTSAT/FY2		G			VIS				IR4

In this document we use DCOMP channel number, this is associated with channel number for each sensor showing in table 1.

DCOMP needs two channels one of visible spectrum (DCOMP ch1 or ch2) and one of the near-IR channels (3-5). We defined DCOMP processing modes 1 to 3 which is associated with DCOMP channels 3 (DCOMP mode 1), 4 (DCOMP mode 2), 5 DCOMP mode 3).

The choice of DCOMP mode can be made by input argument.

## 2 ALGORITHM DESCRIPTION

Cloud optical depth and cloud particle size distribution describe almost completely the radiative properties of a cloud. They characterize the impact of clouds on the energy and radiative budget of the Earth, which is why both properties are used to parameterize clouds in global climate models [Slingo, 1989]. Precise retrievals are critical to improving climate models.

Knowing a measure of the size distribution with CPS and a measure of the vertical thickness of a cloud column given by COD also enables retrievals, under certain assumptions, of the amount of water within the cloud. We separate this value into liquid water path (LWP) and ice water path (IWP) to correspond with the dominant water phase in the cloud.

Note, that within this documentation the term “Cloud Particle Size” (CPS) is synonymous with cloud effective radius and vice versa. Cloud particle size distribution can be represented by the cloud effective radius (REF), which is defined by the integral over the third moment of the distribution over its second moment. This definition makes it clear, that REF is an effective parameter for size distribution for remote sensing problems. Since the definition represents the ratio from the distribution volume of the cloud particles over its cross-area, it shows one of the fundamental topics, the separation of absorption and scattering processes. Clouds can have very different particle size distributions, but effective radii determine the impact on the measured radiance field.

When discussing the scientific background of the algorithm, we will use the term cloud effective radius with the mathematical symbol  $r_e$  to be consistent with other scientific publications. In all sections dealing with the processing and technical details of the algorithm, we will use the term CPS.

DCOMP has been developed at CIMSS and is described in [Walther and Heidinger, 2012].

DCOMP is based on earlier methods that also retrieve cloud optical depth and cloud effective radius from visible and near-infrared wavelengths [Nakajima and King, 1990] [King, 1987; Nakajima and King, 1992]. To briefly describe the underlying idea of the retrieval, cloud optical depth, referred to absorption-free wavelengths (for instance to 550 nm), is determined by the amount of light scattering by cloud droplets. The size of the droplets is responsible for absorption and the transition to a new direction of scattered photons, expressed by the phase function  $P(\zeta)$ , which is a function of the scattering angle,  $\zeta$ . Since REF is a measure of the volume of cloud particles, it is mirrored in absorption amount of clouds. The basic premise is that COD and CPS are inferred from solving the radiative transfer equation for a single-layered, plan-parallel homogeneously distributed cloud above a Lambertian surface. The retrieval concept is based on a 1D radiation concept where a cloud completely covers a pixel.

The DCOMP algorithm uses an absorption-free channel to retrieve the cloud optical depth by measuring upward backscattered radiance and uses an absorption solar channel to estimate particle size through the observed amount of absorption. Simultaneous measurements are required since estimating optical depth from backscattered signals requires the phase function. The amount of absorption cannot be separated from extinction by scattering without measurements in a conservative channel, such as the ABI channel 2.

The cloud optical thickness and cloud particle size are retrieved from measurements of the DCOMP channels 1 centered in the visible spectra at  $\lambda_{VIS} = 0.64 \mu m$  and and DCOMP channel 2, 3, 4 or 5 in the near-infrared spectra at  $\lambda_{NIR} = 1.60 \mu m, 2.25 \mu m, 3.75 \mu m$ . Cloud water content (e.g. LWP/IWP) can be retrieved with some simple assumptions of vertical distributions of cloud droplets with COD/CPS products.

An adequate transformation scheme is established to transform the radiance measurements into reflectivity quantities by considering the geometrical constellation. A doubling/adding radiative transfer model (RTM) is used to solve the forward problem, i.e., the derivation of satellite sensor signals (radiance) by simulating the transfer of solar radiation through the atmosphere for given cloud parameters. Additionally, the RTM calculates transmittance and spherical albedo of a cloud layer. Inferring the optical properties from measured satellite radiances is called the inverse problem. This problem will be managed by a 1D-var optimal estimation approach. A priori assumptions and covariance matrices depend on prior knowledge of climate data sets.

The current COD/CPS algorithm is implemented in the NOAA/NESDIS AIT processing framework. Its routines are used to provide all of the observations and ancillary data in advance of the COD/CPS algorithms. The algorithm is designed to run on segments of data where a segment is comprised of multiple scan lines.

The retrieval strategy includes in general:

- Applying a radiative transfer model to quantify the influence of the cloud microphysical parameters on the backscattered solar radiation measured at the sensor.
- Generating look-up-tables (LUT) for cloud reflectivity, cloud transmission, spherical albedo and cloud albedo of one channel in visible spectrum at  $0.6\ \mu\text{m}$  and for one near-infrared channel at either  $1.6\ \mu\text{m}$ ,  $2.2\ \mu\text{m}$  or  $3.75\ \mu\text{m}$  in respect to DCOMP mode from 1 to 3 for a wide range of possible sun/sensor geometry constellations.
- Receiving from the processing framework all other cloud related derived products (cloud mask, cloud height, and cloud phase) and ancillary data needed by the COD/CPS algorithms.
- Using 1D-var optimal estimation inversion techniques to retrieve the optical thickness and particle size from LUTs of channel reflectivity based on optimal estimation method.

Since the algorithm is mainly pixel-based, it is not sensitive to the choice the segment size. DCOMP does not suffer from edge effects directly. In its current operation, we run the daytime COD/CEPS on segments that contain 200 scan-lines. The only reason to consider a different size may be memory use or as required by other algorithms run in parallel.

## 2.1 Processing Outline

The processing outline of the DCOMP is summarized in Figure 2. The daytime DCOMP algorithm is designed to run on segments (arrays) of data where a segment is comprised of multiple scan lines.

The current DCOMP algorithm can be implemented in several processing environments, such as CLAVR-x, GEOCAT and AWG AIT framework. Those systems provide all primary sensor inputs and ancillary data and generate the output files. The DCOMP algorithm can run on segments of data, as all cloud algorithms do, but can also run on individual pixels if all of the input data and ancillary data sets are available.

The DCOMP retrieval needs the following products from other cloud retrievals: cloud mask, cloud top pressure and cloud phase. Under the current processing structure the generation of these products is done in the same process unit in a pre-defined order in advance to the DCOMP retrieval for each segment. The actual DCOMP retrieval starts at the first call (segment) with testing the channel settings and loading all LUTs and the coefficients for water vapor correction in memory. The memory will be freed after the last scan line is completed.

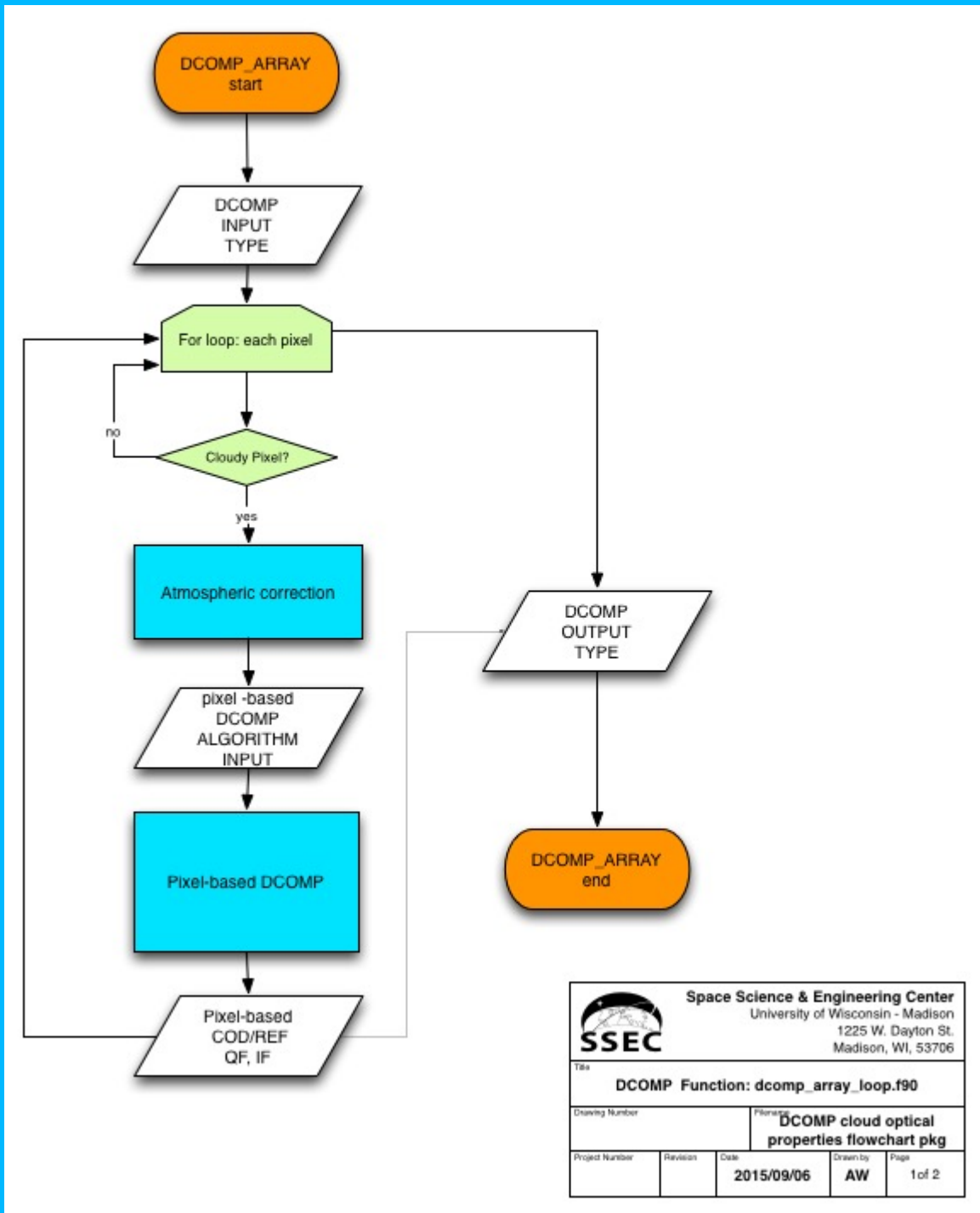
There are two different kinds of look-up-tables (LUT) to be read in. The cloud LUTs include reflection, transmittance, cloud albedo and cloud spherical albedo tables. The ancillary data LUTs include coefficients to estimate transmission in cloud-free layers for ozone and water vapor.

A first test rejects pixels that (1) look into space, are outside valid sensor and sun angle range, are (2) cloud-free, or (3) have no valid cloud pressure or cloud phase. If the input data pass each test, the program sets alias variables for all primary and ancillary input data valid for the current pixel.

Subsequently, atmospheric corrections are executed for the cloud-free layers above and below the cloud (*atmospheric\_correction* subroutine). We correct the atmosphere for the upper layer by estimating the real top-of-cloud reflectance by adjusting the TOA measurement, and by estimating a virtual surface albedo that includes atmospheric extinction for the atmosphere below the cloud. In this way, an observation vector  $y$  is defined as the input of the inversion through an optimal estimation technique with a modified surface albedo. The result of the inversion is a COD/CPS pair from which the liquid water path or ice water path will be calculated, respectively. Those four products and a common quality flag are stored in the output arrays.

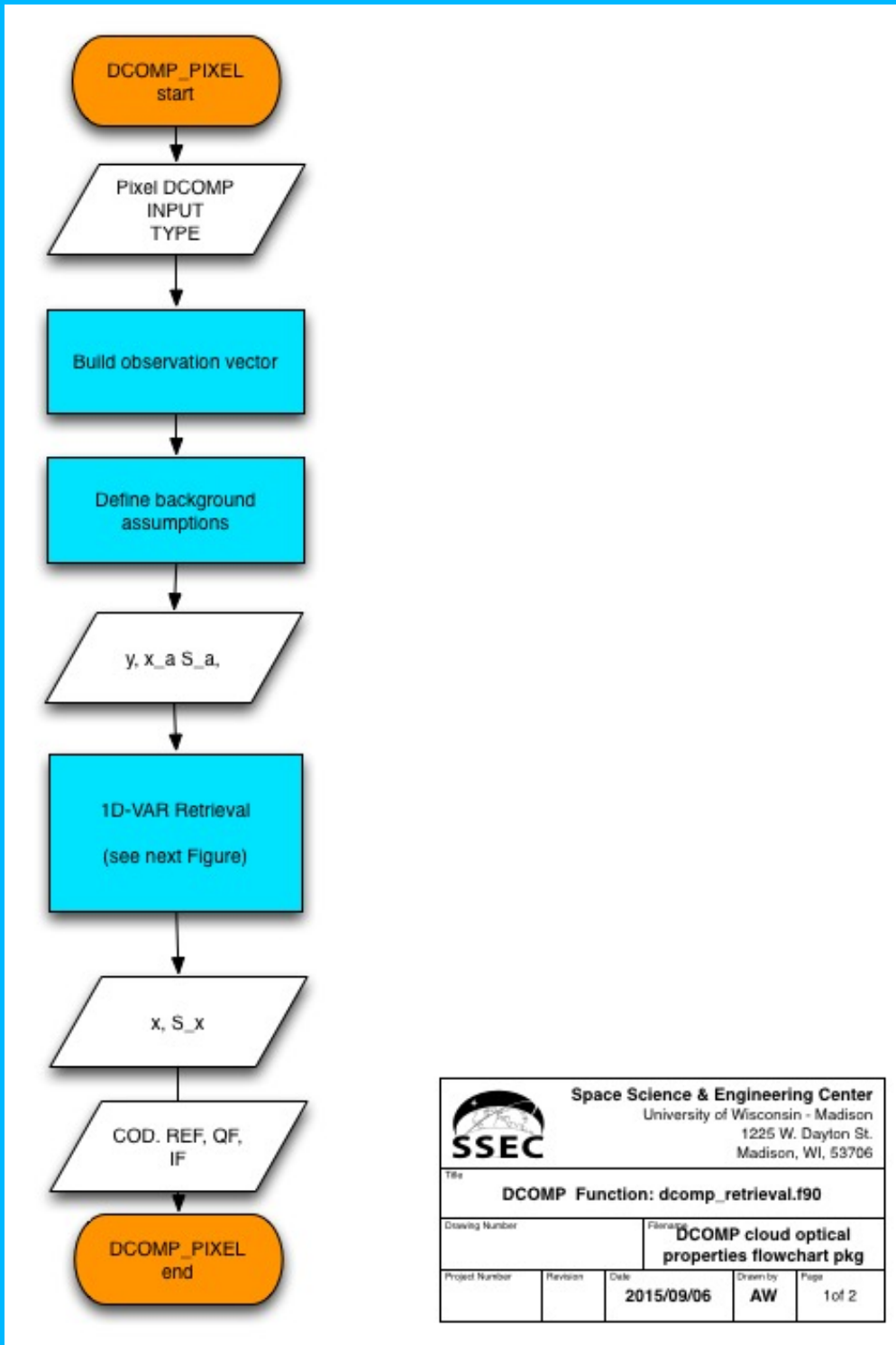
Within the retrieval loop (*optimal\_estimation*), an iterative 1D-var optimal estimation technique is applied (OE). It starts with the definition of a priori values of the state vector and the appropriate observation and atmospheric state covariance matrices. The cost will be calculated for each iteration step. The cost parameter updated at each iteration is initialized with the biggest possible value for this data type (cost = HUGE() for FORTRAN). Each iteration step of the retrieval loop requires search events in the LUTs. Comparison of the TOC reflectance (the observation vector), derived by the forward model represented by the LUTs, to the measurement defines a cost surface function. The OE algorithm's task is to find the minima value on this surface. The gradient of the cost serves as a compass pointing downhill to the deepest point. The a priori values can be seen as a weighting function for the cost surface and help to speed up the state vector journey.

If the cost falls below a pre-defined threshold, the solution is found and the retrieval loop will end. Otherwise, if a maximal number of iterations is exceeded, no solution could be found. The quality flag gets a corresponding value.



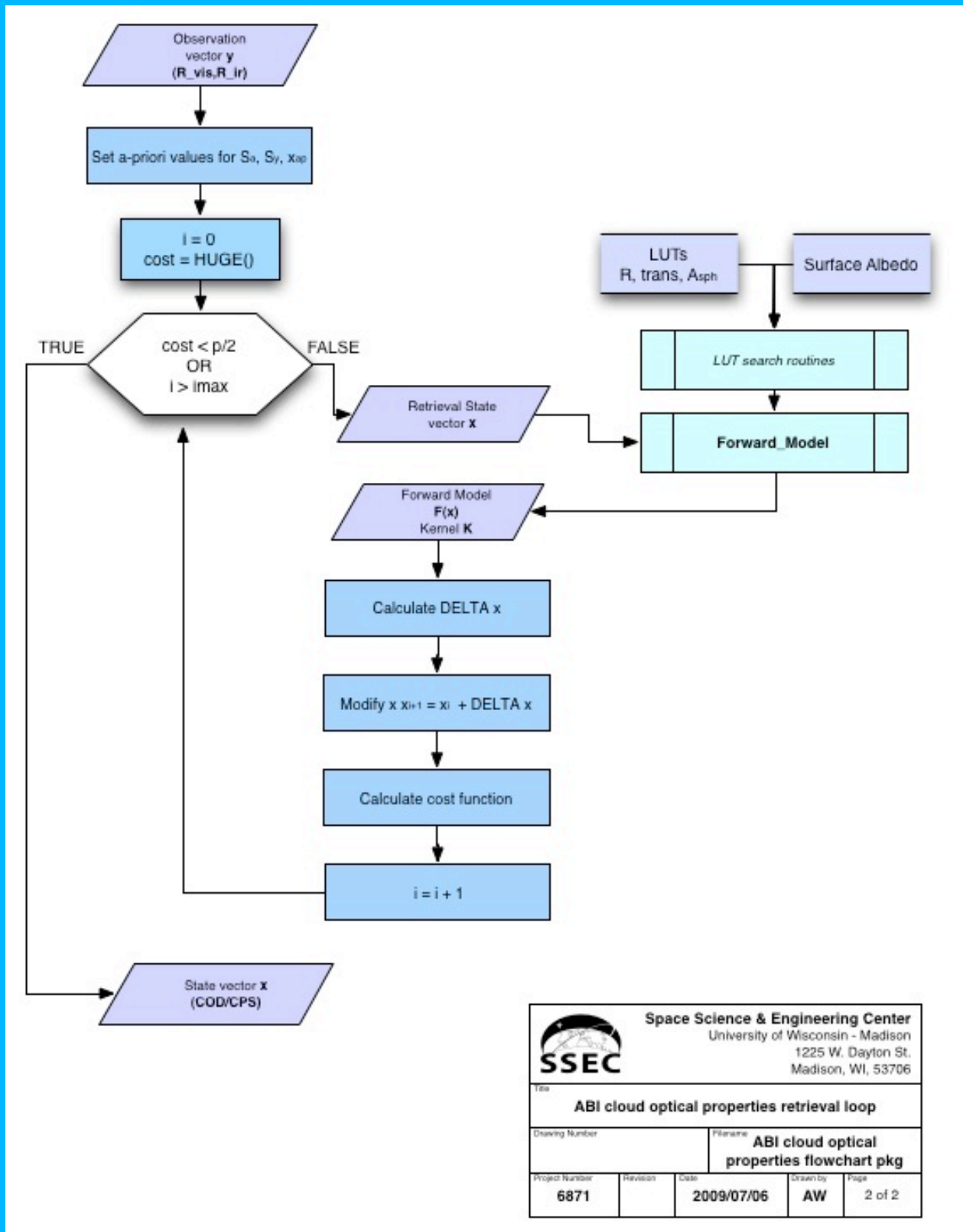
 <b>Space Science &amp; Engineering Center</b> University of Wisconsin - Madison 1225 W. Dayton St. Madison, WI, 53706				
Title				
DCOMP Function: dcomp_array_loop.f90				
Drawing Number		Filename		
		DCOMP cloud optical properties flowchart pkg		
Project Number	Revision	Date	Drawn by	Page
		2015/09/06	AW	1 of 2

Figure 2 High-level flowchart of the DCOMP algorithm.



 <b>Space Science &amp; Engineering Center</b> University of Wisconsin - Madison 1225 W. Dayton St. Madison, WI, 53706		Title	
		DCOMP Function: dcomp_retrieval.f90	
Drawing Number		Filename	
		DCOMP cloud optical properties flowchart pkg	
Project Number	Revision	Date	Drawn by Page
		2015/09/06	AW 1 of 2

Figure 3 DCOMP: Pixel-based flow chart



 <b>Space Science &amp; Engineering Center</b> University of Wisconsin - Madison 1225 W. Dayton St. Madison, WI, 53706				
Title				
ABI cloud optical properties retrieval loop				
Drawing Number		Filename		
		ABI cloud optical properties flowchart pkg		
Project Number	Revision	Date	Drawn by	Page
6871		2009/07/06	AW	2 of 2

Figure 4 Flow chart of 1D-Var inversion retrieval loop.

## 2.2 Algorithm Input

This section describes the input needed to process the DCOMP. As previously mentioned, the embedding processing system (e.g. CLAVR-x, GEOCAT) provides the required cloud mask, cloud type, and cloud height products to the DCOMP algorithm. It is possible to run the program as a stand-alone code if cloud mask, cloud phase and cloud height data are obtained from a different source.

DCOMP input is defined in interface structure in software file *dcomp\_interface\_types\_mod.f90*. The following subsections sub-classify the input in functional groups.

### 2.2.1 Control parameters

The input structure consists on three control parameters:

	Data type	Description	Dimension
<i>mode</i>	integer	DCOMP mode 1, 2 or 3	scalar
<i>lut_path</i>	string	Path location where LUTs are stored	scalar
<i>Sensor_wmo_id</i>	integer	WMO ID for sensor	scalar

### 2.2.2 Primary Sensor Data

The list below contains the primary sensor data used by DCOMP retrieval. Primary sensor data refers to information that is derived solely from the ABI observations and its associated geo-location information. The DCOMP algorithm uses calibrated reflectance percent (0-100) for each visible/near-IR channel as input.

While the input array has the same dimensions for reflectance and radiance for better readability, reflectance has only valid values for solar channels, and radiance has only valid values for thermal channels.

The relative azimuth difference definition follows the “follow the photon” convention. (If sun and sensor appears at the same spot of the sky for an observer on Earth, we have a relative azimuth difference angle of 180 degree)

**Table 3 DCOMP primary sensor input**

Variable Name	Data type	Description	Dimension
<i>refl</i>	Real4	Calibrated reflectance	grid (n_chan,x, y)
<i>rad</i>	Real4	Calibrated radiance	grid (n_chan,x, y)
<i>sol</i>	Real4	Solar zenith angle	grid (x, y)
<i>sat</i>	Real4	Sensor view zenith angle	grid (x, y)
<i>azi</i>	Real4	Relative azimuth difference	grid (x,y)

### 2.2.3 Ancillary Data

The following data lists the ancillary data required to run the DCOMP algorithm. By ancillary data, we mean data that requires information not included in the sensor observations or geo-location data. Ancillary data includes data such as land and snow masks, NWP and RTM data as well as the lookup tables (LUT) that are used in the forward model calculations. The NWP and RTM data, which are at NWP resolution, has to be interpolated to pixel level in the processing system. The NWP is used as a backup in case the IMS snow mask is not available. Table 4 lists the non-LUT data, which are used in DCOMP. Table 5 lists the NWP data that are used in DCOMP and Table 6 lists the information in the DCOMP LUT. Table 5 summarizes data source of ancillary data and cloud products as used for Clavr-x version of DCOMP.

- **Land mask**  
A land mask has to be applied in the processing system and has to be passed to DCOMP as a Boolean variable with “true” standing for land surface.
- **Information whether this pixel should be run in DCOMP**  
The embedding retrieval system detects pixels, which cannot be run in DCOMP due to missing or bad-quality information or input data or other reasons. This information is provided by logical data type “is\_valid”. If this input variable is set to FALSE DCOMP won’t start for this pixel.
- **Surface clear sky reflectance (Albedo)**  
The MODIS surface albedo product for all visible channels is used.
- **Snow Mask**  
Current version uses NWP CSFR snow mask. Other options are GlobSnow and every available sensor-specific snow product. The current version only uses snow/ snow-free information. In a future version there might be more snow classes applied.
- **Numerical weather prediction (NWP) data:**  
NWP data are used to estimate the absorber mass for atmospheric correction of water vapor and ozone absorption, snow class and the determination of surface pressure for aerosol and Rayleigh correction. DCOMP uses the same ancillary data as all cloud algorithms.

**Table 4 Ancillary input data**

Variable Name	Data type	Description	Dimension
<i>is_land</i>	Boolean	If land set to “true”	grid (x, y)
<i>Is_valid</i>	Boolean	If valid pixel set to “true”	grid (x, y)
<i>snow_class</i>	Int1	Snow class	grid (x, y)
<i>alb_sfc</i>	Real4	Surface albedo	grid (n_chan,x, y)
<i>press_sfc</i>	Real4	Surface pressure	grid (x,y)
<i>emiss_sfc</i>	Real4	Surface emissivity	Grid(n_chan,x,y)
<i>Sun_earth_distance</i>	Real4	Sun Earth distance in AE	scalar

**Table 5 Source and reference of ancillary and cloud product data**

Forward model parameter	Data source	Reference
Surface albedo	MODIS white sky albedo	(Moody et al. 2008; Schaaf et al. 2002)
Phase function water	Doubling-adding RTM/ Mie calculations	(Wiscombe 1980)
Phase function of ice clouds	Baum and Yang data base	(Baum et al. 2005)
Atmospheric profiles	NCEP CFSR	(Saha et al. 2010)
Cloud phase	Clavrx-x cloud type algorithm	(Pavolonis et al. 2005)
Cloud top pressure	Clavrx-x cloud height retrieval ACHA	(Heidinger and Pavolonis 2009)
Cloud mask	Clavrx-x cloud mask retrieval	(Heidinger et al. 2012)

#### 2.2.4 Pre-derived Data

The following lists and briefly describes the data that are required by DCOMP that are provided by other cloud product algorithms. The data source and references are listed in Table 5.

- Cloud mask**  
 A cloud mask is required to determine which pixels are cloudy and which are cloud free, which in turn determines which pixels are processed. Details on the cloud retrieval should be provided in a cloud mask ATBD.
- Cloud top pressure, cloud top temperature**  
 Cloud top pressure is required to determine the amount of absorber mass by water vapor and other gases above the cloud for atmospheric correction. While within CLAVR-x the retrieval ACHA is used, also other cloud height retrievals can be used for this input. Details are described by corresponding ATBD, which is done for ACHA in the ACHA ATBD
- Cloud phase**  
 Cloud phase is required to determine which LUT, ice or water is used for forward model calculations. A Cloud type/Phase algorithm provides this information. The Cloud Type/Phase ATBD provides details on the Cloud Type/Phase.
- Cloud optical thickness from IR method**  
 This is an optional output to include IR method to retrieve COD. This is only possible for thin cirrus clouds and builds the first-guess for thin cirrus clouds.

**Table 6 DCOMP input: Derived cloud products.**

Variable Name	Data type	Description	Dimension
<i>cloud_mask</i>	Int1	Cloud mask	grid (x, y)

<i>Icloud_type</i>	Real4	Cloud type	grid (x, y)
<i>Cloud_temp</i>	Real4	Cloud top temperature	grid (x, y)
<i>Cloud_press</i>	Real4	Cloud top pressure	grid (x,y)
<i>tau_acha</i> *	Real4	COD from IR method	grid (x,y)

\* optional, this is used for first guess for thin cirrus clouds.

### 2.2.5 Look-up-tables

Look-up-tables are provided for cloud properties and for atmospheric transmission coefficients. The LUTs, which are instrument specific, are generated in advance and are static ancillary data. The LUT generation is described more in detail in section 2.3.2.1. Cloud properties LUT set consists of four data files for ice and water phase and for both channels. Transmission coefficients are provided in one LUT file.

**Table 7 LUT ancillary data**

Name	Type	Description	Dimension
Cloud properties LUT	Input	Cloud reflectance as a function of effective radius, optical depth, solar zenith angle, local zenith angle and relative azimuth difference angle	(9 x 29 x 45 x 45 x 45)
		Cloud transmission as a function of effective radius, cloud optical depth and incoming angle	(9 x 29 x 45)
		Cloud spherical albedo as a function of effective radius and cloud optical depth	(9 x 29)
		Cloud albedo as a function of effective radius and cloud optical depth	(9 x 29 x 45)
Transmission coefficients LUT	Input	Three ozone transmission coefficients for channel 2	3
		Three water vapor transmission coefficients for channel 2 and 6.	(2 x 3)

## 2.3 Theoretical Description

For better readability and to be consistent with other publications, the terms cloud optical depth and effective radius are represented by the mathematical symbols  $\tau_c$  and  $r_e$ , respectively.

### 2.3.1 Physics of the Problem

**Table 8 Parameters and mathematical symbols used in Chapter 3.4.1**

Parameter	Symbol	Typical Value
-----------	--------	---------------

Reflectance ( at top of atmosphere, top of cloud)	$R$ ( $R_{TOA}, R_{TOC}$ )	0.4
Reflectance backscattered to sensor	$R_{sc}$	0.1
Transmittance function (above, below cloud)	$T(T_{ac}, T_{bc})$	0.95
.. through water vapor including trace gases	$T_{h_2o}$	0.91
.. through ozone, aerosol, air molecules	$T_{o_3}, T_{aer}, T_r$	0.93
.. for cloud, downward, cloud upward	$T_c, T_c^*$	0.8, 0.8
Local zenith angle, cosines of	$\theta, \mu$	34, 0.7
Solar zenith angle, cosines of	$\theta_0, \mu_0$	34, 0.7
Relative azimuth difference	$\Delta\varphi$	120
Optical depth for clouds, Rayleigh, aerosol	$\tau_c, \tau_r, \tau_{aer}$	12 0.03 0.05
Background optical depth for Rayleigh, aerosol	$\tau_{r,0}, \tau_{aer,0}$	0.044 0.1
Cloud, particle radius, Effective radius	$r, r_e$	10 $\mu m$
Cloud droplet number distribution	$n(r)$	1000
Phase function	$P$	0.3
Rayleigh phase function	$P_r$	0.2
Scattering angle	$\zeta$	123 deg
Cloud albedo	$A_c$	0.4
Spherical cloud albedo	$R_c^*$	0.1
Azimuthal averaged reflectance	$R^*$	0.1
Air mass factor	$AMF$	2.9
Asymmetry parameter	$g$	0.7
Single-scattering albedo	$\omega_0$	1
Surface pressure, cloud top pressure	$P_{sfc}, P_c$	540hPa 1013hPa
Solar radiation	$I$	
Surface Albedo	$A_{sfc}$	0.08

---

### 2.3.1.1 Basic Considerations

Cloud radiation characterizations in the shortwave range of the infrared spectrum are almost exclusively a function of cloud optical depth (also referred to as cloud optical thickness) and the cloud droplet distribution  $n(r)$ , which can be represented by the integral of the third moment over the second moment of the distribution of particle size, the effective radius  $r_e$  [Hansen and Travis, 1974]:

$$r_e = \frac{\int r^3 n(r) dr}{\int r^2 n(r) dr} \quad (1)$$

It has been shown that the effective radius represents adequately the radiative properties of a cloud, which are largely independent to the shape and width of the droplet distribution. The values of effective radius vary usually between  $r_e = 3 \mu m$  and  $r_e = 40 \mu m$  for liquid cloud phase

and up to  $r_e = 100 \mu m$  for ice clouds. As a simplification, cloud optical depth determines the quantity of scattering processes, while cloud droplet size is responsible for redistributing the direction of the scattering processes, expressed as the phase function  $P(r)$ . Cloud optical depth and effective radius are often used for the characterization of clouds in global climate models. Both together describe completely the backscatter signature of a cloud.

For the retrieval instead of a measured direct solar reflected radiance  $L [Wm^{-2}nm^{-1}sr^{-1}]$ , we use a measure of reflectivity  $R$  for each wavelength. Those values may be calculated under consideration of the spectral solar constant  $F_0 [Wm^{-2}nm^{-1}]$ , the sun zenith angle  $\theta_0$  and the local zenith angle  $\theta$  as

$$R(\theta_0, \theta, \lambda) = \frac{\pi L(\theta_0, \theta, \lambda)}{F_0(\lambda) \cos \theta_0} \quad (2)$$

By using  $R$  instead of  $L$  we avoid an overestimation of shortwave channels, where the solar irradiance is bigger than for longer wavelengths.

Cloud optical depth represents optical characterization at visible wavelengths and can be expressed as a function of the scattering coefficient  $Q$ , the droplet size distribution  $n(r)$  and the droplet radius  $r$ :

$$\tau = \int n(r)Q(r, \lambda)\pi r^2 dr \quad (3)$$

The cloud liquid water path may be derived with the cloud optical thickness and the droplet effective radius estimates using the following equation [Stephens, 1978] , [Bennartz, 2007]

$$LWP = \frac{5}{9} \tau_c r_e \rho \quad (4)$$

where  $\rho$  is the density of liquid water.

The ice water path (IWP) can be derived by (Heymsfield, 2003):

$$IWP = \frac{\tau_c^{1/0.84}}{0.065} \quad (5)$$

This relationship fits the observations for several locations and experiments, as described in the Heymsfield paper. Eq. (5) leads to big differences in comparison to traditional methods which use a small dependency to cloud particle size similar to the equation for liquid phase. Figure 4 shows big differences in the retrieved IWP product for different methods.

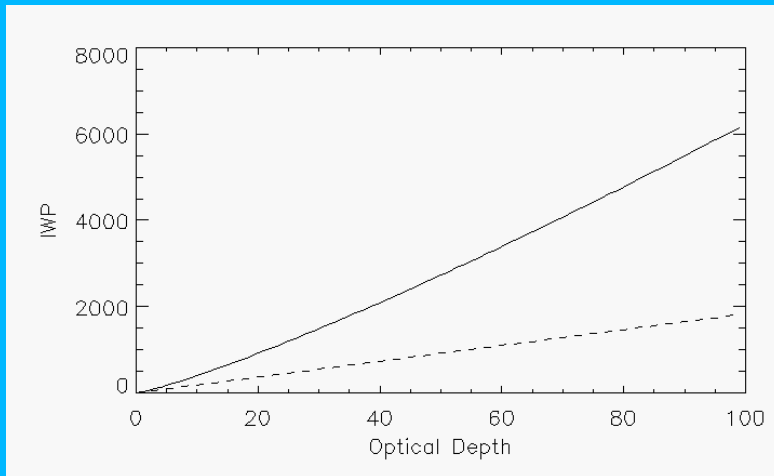


**Figure 5 Comparison of Heysfield method to a traditional method (dashed line) of calculating the ice water path from optical depth.**

It has been shown that using two channels in the visible and near infrared spectrum is sufficient to retrieve both parameters (King 1987, Nakajima und King 1991). The underlying principle on which these methods are based is the fact that the cloud reflectance at visible wavelengths is primarily a function of the cloud optical thickness, while the variations in the measured reflectance in the near infrared water-absorbing channels are mostly affected by the particle size. The basic premise is that DCOMP is inferred from solution of the radiative transfer equation for a single-layered, homogeneously distributed cloud above a Lambertian (isotropic) surface. A cloud with a given optical thickness and cloud effective particle size can be described by its reflectance/transmittance functions. To speed up the process for operational retrievals, the reflectance/transmittance functions for both ice and water clouds are pre-calculated and stored in look-up tables (LUTs). Further description of the process used to develop the LUTs is given in the following section, as is the methodology to use the LUT to infer COD/CPS.

### 2.3.1.2 Radiative Transfer Calculations

To simulate the radiative properties of a cloud, a doubling-adding model is used. In this model the atmosphere comprises three layers, two cloud-free layers and a cloud layer in between. The doubling-adding method to solve radiative transfer problems is widely used in the scientific community. Van de Hulst developed this technique. It generates fast and accurate estimates of light distribution in a cloudy atmosphere. It assumes knowledge of the reflection and transmission properties for a single thin homogeneous atmosphere layer. The basic principles can be found in several publications, such as Goody and Young van de Hulst or Thomas and Stamnes. These calculations generate look-up tables of cloud parameters. The LUTs are static and will be provided as ancillary data.

A general expression for the radiative transfer in the absence of thermal emission within the atmosphere can be formulated as:

$$\mu \frac{dI(\mu, \varphi)}{d\tau} = I(\mu, \varphi) - \frac{\omega_0}{4\pi} \int_0^{2\pi} \int_{-1}^1 P(\mu, \varphi, \mu', \varphi') I(\mu', \varphi') d\mu' d\varphi' \quad (6)$$

Measured attenuation of solar radiance is a function of the single scattering albedo  $\omega_0$ , the scattering phase function  $P$  and the incoming solar radiation  $I$ . The reflected solar radiance at wavelength with no thermal emissions is a result of absorption and scattering processes within clouds and at the surface. Extinction in visible wavelengths is caused by scattering directly proportional to scattering cross-area. The size of cloud particles determines the shape of the scattering phase function and is therefore essential to retrieve the angular distribution of backscattered light. The amount of absorption in channel 6 is directly proportional to the absorber volume. Extinction in absorbing channel is influenced by water absorption and thus, is a function of cloud particle size. The simultaneous retrieval of COD and CPS is required since scattering and absorption partition on extinction can otherwise not be separated.

Radiative transfer simulations have been performed to create a dataset as a basis for the forward calculations during the inversion process. They should cover the entire range of possible conditions and account for all parameters and processes, affecting the retrieval. The RTM needs single scattering phase functions for water and ice droplets. Water particles were taken to be composed of spherical droplets at all wavelengths and Mie scattering ([Wiscombe, 1980]) was assumed for the inference of scattering and absorption properties.

For a given droplet size distribution and optical constants of water, a Mie-code returns extinction and scattering coefficients and the scattering phase function, which describes the angular distribution of scattered light in a single scattering event. The droplet size distribution is approximated by an analytical function, the modified Gamma-Hansen function

$$n(r) = r \frac{1-3r_b}{r_b} e^{-r/r_b} \quad (7)$$

which is determined by two parameters: the effective radius  $r_e$  and a dispersion  $r_b$  about the effective radius. We assume for the dispersion (that is mean effective variance, a measure for the distribution width) a value of 0.1.

The RTM employs a delta-M scaling of the phase function. The model runs with a dataset on atmospheric temperature and cloud microphysical properties. Clouds are treated as plane parallel homogeneous layers of water, ice or liquid, droplets. The optical properties of the droplet size distribution are parameterized in terms of the effective radius.

A single-layered fast RTM is used for simulating the reflectance at the top of the atmosphere (TOA) for the ABI solar and near-infrared channels. The atmosphere in this model is divided into two cloud-free layers with a cloud layer between and a non-reflecting surface.

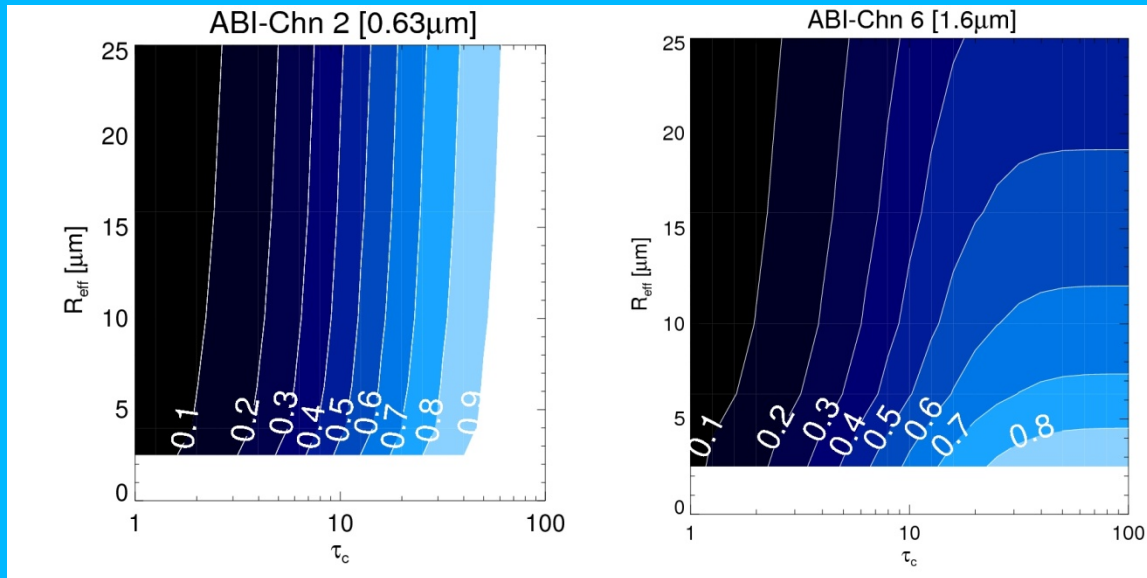


**Figure 6** Example of simulated cloud reflectances as a function of optical depth and effective radius for DCOMP channel 1 (ABI-channel 2; left) and DCOMP channel 3 (channel 5; right). Satellite zenith is 20, Local zenith angle = 20 and Relative azimuth angle = 140.

Figure 5 illustrates that the reflectance in non-absorbing ABI channel 2 is primarily a function of cloud optical thickness. The reflectance is almost fully explained by the variations in optical depth, there is only weak sensitivity to effective radius. The right panel of Figure 5 shows that reflectance in Channel 6 is also highly sensitive to cloud optical thickness for thin clouds with  $\tau_c < 10$ . At thicker clouds this behavior changes to a higher sensitivity to effective radius.

The situation for ice clouds is more complex as the particles are generally not spherical. The assumption of spherical particle shapes for the ice phase leads to substantial errors [Mishchenko *et al.*, 1996]. Ice clouds are currently composed of a mixture of habits consisting of droxtals (primarily for the smallest particles in a size distribution), hollow and solid columns, plates, 3D bullet rosettes, and aggregates. Current research activities are underway to implement 3D bullet rosettes with hollow bullets, which more closely approximate those observed in ice clouds. The hollow bullet rosettes also have very different scattering/absorption properties than those of solid bullet rosettes.

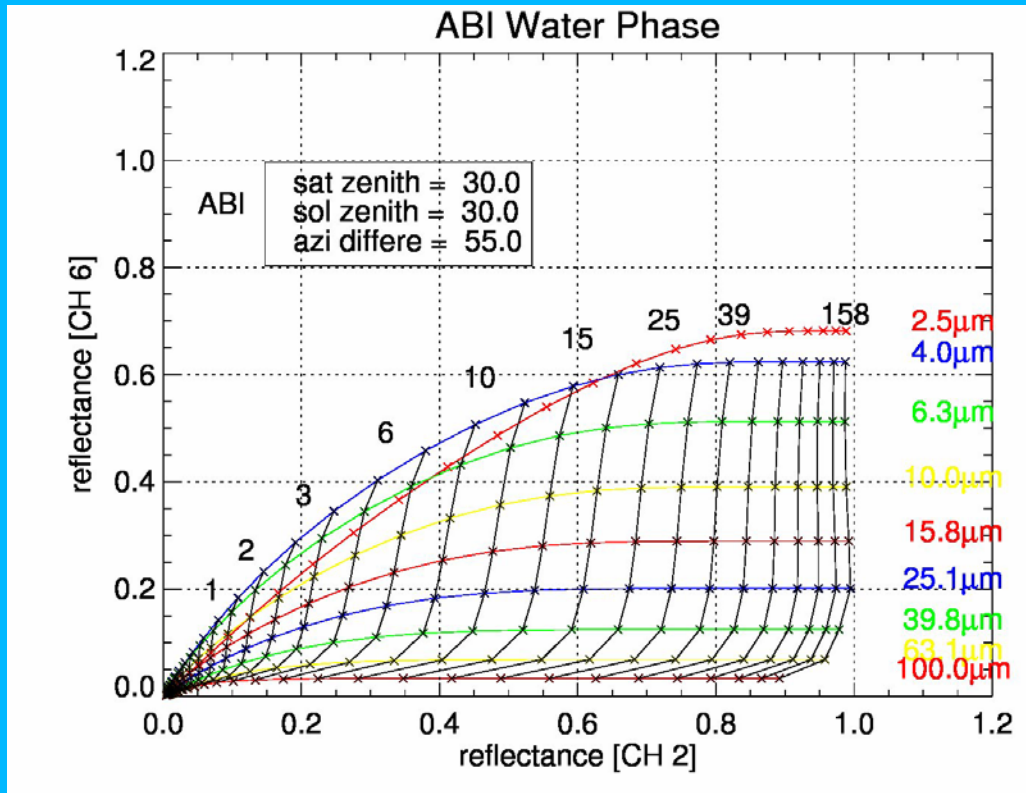


Figure 7 Theoretically computed cloud reflectance function for water phase of GOES-ABI channels 2 and 6 (DCOMP channel 1 and 3) for an arbitrary geometrical observation constellation.

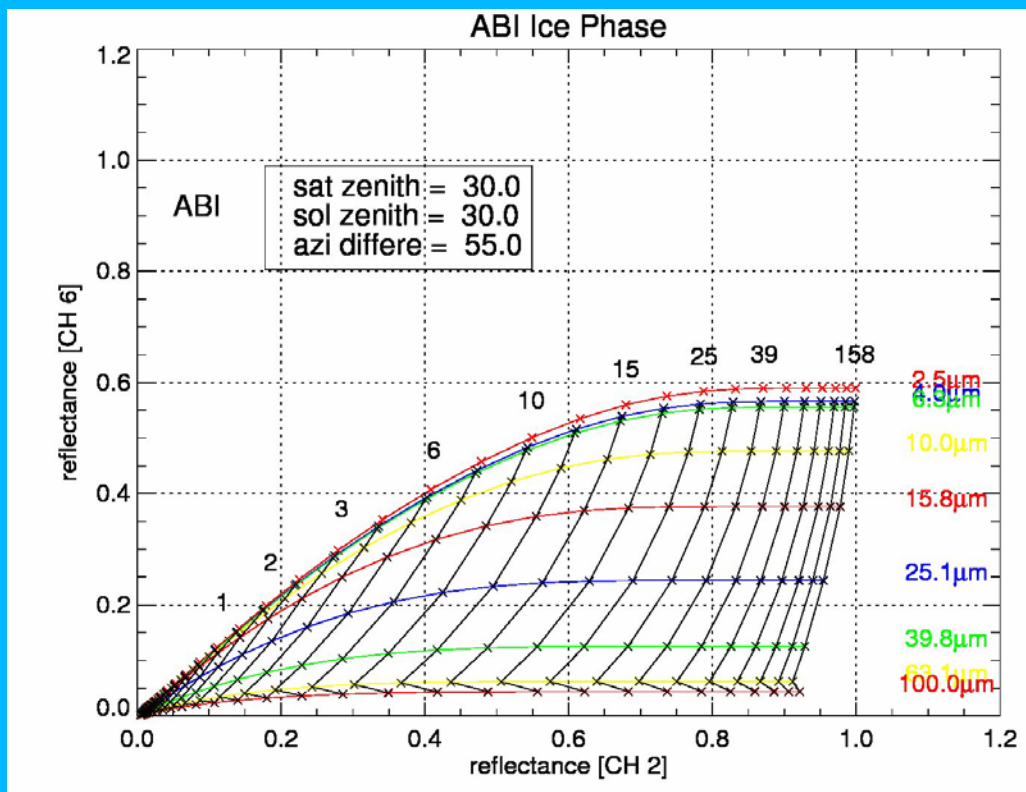


Figure 8 Same as Figure 6 , but for ice clouds.

Figure 6 and Figure 7 show visualizations of the cloud reflectance function for an arbitrarily chosen observation geometry for ice and water clouds. Colored lines are the iso-lines of effective radius and black lines are the iso-lines of cloud optical depth. The line of equal 2.5 micron effective radius in the water cloud image crosses isolines of bigger particle distributions. The solution for measured reflectance values in this region is ambitious.

The following cloud parameters are extracted from the simulation output:

- **Cloud reflectance:** The cloud reflectance  $R_c$  is a function of observation geometry and the cloud parameters  $\tau_c$  and  $r_e$ . It denotes the bidirectional reflectance function of the cloud for light coming from above (i.e., the Sun). The RTM is able to calculate the radiative flux at any level in the atmosphere. The ratio between incoming and outgoing radiation at solar zenith, local zenith and azimuth angles denotes the cloud reflectance, as defined in

Eq. (2).

$$R_c(\tau_c, r_e, \theta_0, \theta, \Delta\phi) = \frac{\pi L \uparrow(\tau_c, r_e, \theta_0, \theta, \lambda)}{F_0(\lambda) \cos \theta_0} \quad (8)$$

- **Cloud transmission:** Cloud total transmission (diffuse plus direct) is calculated by computing the ratio of solar flux and the measured radiance below the cloud in the incoming path direction:

$$T_c(\tau_c, r_e, \theta_0) = \frac{\pi L \downarrow(\tau_c, r_e, \theta_0)}{F_0(\lambda) \cos \theta_0} \quad (9)$$

- **Cloud albedo:** Cloud albedo, also referred to plane albedo, depicts the overall backscattered radiance at a cloud level:

$$A_c(\tau, r_e, \mu_0) = \frac{1}{\pi} \int_0^{2\pi} \int_0^1 R_c(\tau, r_e, \mu, \mu_0, \Delta\phi) 2\mu_0 d\mu d(\Delta\phi) \quad (10)$$

- **Cloud spherical albedo:** Cloud spherical albedo is found by integrating the outgoing radiance over all azimuth angles as:

$$R_c^*(\tau_c, r_e) = \frac{2}{\pi} \int_0^1 \left[ \int_0^{2\pi} \int_0^1 R_c(\tau_c, r_e, \mu, \mu_0, \Delta\phi) \mu d\mu d(\Delta\phi) \right] d\mu_0 \quad (11)$$

LUTs for both water and ice clouds that contain all cloud parameters described above for relevant ABI channels were generated. The reflectivity LUTs are computed assuming a cloud above a non-reflecting (black) surface. With this simplified approach, there is no atmosphere and also no aerosols in the layers above and below the cloud layer. Nor is there multiple scattering between the cloud and a reflecting surface.

### 2.3.1.3 Impact of Surface Reflection

We consider the cloud as a single-layer homogeneously distributed cloud layer over a Lambertian surface having an albedo  $\alpha_s$ . The calculations possess reflectance and transmittance functions given by  $R_c(\tau_c, r_e, \mu_0, \mu, \Delta\phi)$  and  $T_c(\tau_c, r_e, \mu_0)$ , where  $\mu$  is the cosine of the local zenith angle,  $\mu_0$  is the cosine of the solar zenith angle, and  $\Delta\phi$  is the relative azimuth angle between the direction of propagation of the emerging radiation and the incident solar radiation, respectively.  $T_c$  denotes the diffuse and direct cloud transmittance for light from above, and  $T_c^*$  for light from below (following King, 1987). The total cloud-surface bidirectional reflectance function  $R$  at the top of the cloud (or atmosphere) can be expressed by:

$$R_{TOC} = R_c + \frac{A_{sfc}}{1 - A_{sfc}R_c^*} T_c T_c^* \quad (12)$$

Since  $R_c^*$  redirects downward the radiation from all incident angles, it is a directionally-integrated parameter; thus, it is only a function of  $\tau_c$  and  $r_e$ . The value  $T_c$  is the cloud downward transmittance at the solar zenith angle  $\mu_0$ . It is a hemispherical-integrated parameter and thus a function of optical thickness, effective particle size, and the solar zenith angle:  $T_c = f(\tau_c, r_e, \mu_0)$ . King (1987) discussed the use of reflected solar radiation measurements to infer  $\tau_c$ . The surface albedo  $A_{sfc}$  is taken from MODIS white-sky albedo maps. If the snow mask detects snow or sea-ice a default value of 0.86 and 0.80 is used, respectively.

### 2.3.1.4 Forward model in near-infrared channel around 3.75 micron

If DCOMP is applied to sensor channels around 3.8 microns (such as AVHRR channel 3b, SEVIRI channel 4, GOES channel 2 or MODIS channel 20) terrestrial emission must be taken into account. The term  $R_{TOC}$  in depicts the solar reflectance. However, for these channels the measured radiance is a sum of backscattered solar radiation and a terrestrial emission part. The latter is the top of cloud radiance  $I_{TOC}$ , which is emitted from the surface and atmosphere. This can be expressed as

$$I_{TOC} = \varepsilon(\tau, r_e) B_c(T_c) + t_c(\tau, r_e)(I_{clr} - I_a(H))$$

where  $I_a$  is the radiance contribution from layers above the cloud height  $H$ ,  $I_{clr}$  is the clear-sky radiance emitted by the surface,  $\varepsilon_c$  is the cloud emissivity,  $t_c$  is the cloud transmission, and  $B(T_c)$

is the Planck function at the cloud top temperature  $T_c$ . Cloud emissivity  $\varepsilon(\tau, r_e)$  and cloud transmission  $t_c(\tau, r_e)$  are computed by the radiative transfer model and stored in look-up-tables.

They depend on the state vector, so that they are optimized during the retrieval loop. The other unknown variables of equation 5 are obtained from auxiliary data as follows. The new National Center of Environmental Prediction (NCEP) Climate Forecast System Reanalysis (CFRSR)

(Kalnay et al. 1990; Saha et al. 2010; Sela 1980) provides realistic atmospheric profiles of temperature and water vapor on global regular 0.5 and 2.5 degree grid from 1979 onwards. We employ a fast IR radiative transfer code, the Pressure-Layer Fast Algorithm for Atmospheric Transmittances PFAAST (Hannon 1996) with the input from these reanalysis, combined with surface emissivity values obtained from a MODIS-based database (Seemann et al. 2008) to compute assumed clear-sky radiance and transmission profiles.

Cloud top temperature and cloud top height are obtained from the AWG Cloud Height retrieval Algorithm (ACHA), which is also part of PATMOS-x retrieval scheme, in which it runs in advance of DCOMP.

Subsequently, the terrestrial radiance  $I$  can be transformed into an equivalent reflectance value

$R_e$  as follows:

$$R_{e,TOC} = \frac{\pi d^2}{\mu_0 F_0} I_{TOC}$$

where  $d$  is the Earth-Sun distance in astronomic units (AU) and  $F_0$  is the channel-specific solar constant normalized to the average Earth-Sun distance using the Kurucz solar irradiance database (Kurucz 1995). The solar part of the measured reflectance are extracted by

$$R_{TOC} = R_{mea} - R_e$$

Through including the terrestrial emissivity observed at top of cloud, Eq. (3) becomes an equation for each measurement channel:

$$R_{TOC} = R_c(\tau, r_e) + \frac{A_v t_{c,0}(\tau, r_e) t_c(\tau, r_e)}{1 - A_v S(\tau, r_e)} + R_{e,TOC}(\tau, r_e)$$

This is in fact a general equation for any channel. For the visible to near-infrared spectral range, the amount of radiance, which comes from surface or atmospheric emission, is negligible, and  $R_{e,TOC}$  becomes zero.

Now all formulations are prepared to proceed to the inversion problem, which aims to find the pair of cloud properties  $(\tau, r_e)$ . At the end of this process the retrieval will find a pair of the cloud properties  $(\tau, r_e)$  that satisfy the equations. The problem is not analytically solvable due to the complicated nature of radiative transfer.

### 2.3.2 Mathematical Description

This section describes the mathematics used by the retrieval, including all simplifications, approximations, and numerical methods. This section is divided in the description of the LUTs as the representation of a forward model, the correction of atmospheric impacts on the measured input data, and the inversion method.

### 2.3.2.1 Structure and Interpolation of LUT Data

Section 3.4.1.2 describes the radiative transfer model used to generate look-up tables. These tables store cloud parameters, which are used for forward model calculations within the retrieval. These computations are carried out in advance. The derived LUTs are provided as ancillary data algorithm input. The access and interpolation of the LUTs are part of the retrieval.

#### 2.3.2.1.1.1 Structure of LUTs

The LUTs are generated both for water and ice clouds. The following DCOMP channel lookup tables will be provided for water and ice clouds.

The following parameters have been included in the lookup table sets.

For water clouds the following set-up is determined:

1. 45 Solar zenith angles: 0 to 88 degrees in steps of 2 degrees.
2. 45 Local zenith angles: 0 to 88 degrees in steps of 2 degrees.
3. 45 Azimuth angle difference: 0 to 170 degrees in steps of 5 degrees  
170 to 180 degrees in steps of 1 degree
4. 9 Effective radii: defined in log10 space  $\rightarrow$  0.4 to 2.0 in steps of 0.2
5. 29 Cloud optical depths: defined in log10 space  $\rightarrow$  -0.6 to 2.2 in steps of 0.1

The set-up for ice clouds is defined as:

1. 45 Solar zenith angles: 0 to 88 degrees in steps of 2 degrees.
2. 45 Local zenith angles: 0 to 88 degrees in steps of 2 degrees.
3. 45 Azimuth angle difference: 0 to 170 degrees in steps of 5 degrees  
170 to 180 degrees in steps of 1 degree
4. 9 Effective radii: defined in log10 space  $\rightarrow$  0.4 to 2.0 in steps of 0.2
5. 29 Cloud optical depths: defined in log10 space  $\rightarrow$  -0.6 to 2.2 in steps of 0.1

As described in Section 3.4.1.2 LUTs are calculated for the

1. Cloud reflectivity function calculated for a non-reflective surface (albedo = 0) as a function of cloud optical depth, effective radius, solar zenith , local zenith and relative azimuth angle difference with a dimension of [45,45,45,9,29];
2. Cloud transmission function as function of cloud optical depth and effective radius and solar zenith angle (dimension [45,9,29]);
3. Spherical albedo as a function of cloud optical depth and effective radius ([9,29]); and
4. Cloud albedo as a function of cloud optical depth and effective radius and incoming angle (9,29,45).

#### 2.3.2.1.1.2 Interpolation

Within the LUTs the values will be searched with linear interpolation for all up to five dimensions. Standard models of linear interpolation are described in the following section.

We must first compute the following quantities with variables  $z$ ,  $w$ ,  $v$  representing the angular input variables (solar zenith, satellite zenith and relative azimuth difference) in case they are part of the LUT input for this simulation output.

For convenience and computational efficiency the individual LUTs are transformed in a smaller array with sub-arrays of all inputs:

$$\begin{aligned}
 R_c^{sub} &= (r_{ijklm}) \subset R_C \\
 i &= \{x_1; x_2\}; j = \{y_1, y_2\}; k = \{w_1, w_2\}; l = \{v_1, v_2\}; m = \{z_1, z_2\} \\
 T_c^{sub} &= (r_{ijk}) \subset T_C \\
 i &= \{x_1; x_2\}; j = \{y_1, y_2\}; k = \{w_1, w_2\} \\
 S^{sub} &= (r_{ijk}) \subset S \\
 i &= \{x_1; x_2\}; j = \{y_1, y_2\}; k = \{w_1, w_2\}
 \end{aligned} \tag{13}$$

where  $x_1, x_2$  are the next lower and upper LUT entrée index for the input value of the first dimension of the LUT. This is also set for the other dimensions with variables  $y$ ,  $w$ ,  $v$ ,  $z$ . The quantities in the following describe the relative distance of the input value to the next LUT entrees for the respective dimension.

The following pseudo code fragments show the interpolation scheme for DCOMP.

- Interpolation over 5 dimensions can be carried out as written in a pseudo code fragment in the following. Let's consider the matrix A5 as a five-dimensional array. The matrix A4 is the matrix for which the 5<sup>th</sup> dimension of A5 was interpolated.

---

**Pseudo code algorithm:** Interpolation 5D

---

**FOR** each element of first dim = i  
**FOR** each element of second dim = j  
**FOR** each element of third dim = k  
**FOR** each element of fourth dim = m

$$A4 [i, j, k, m] = p5 * A5 [i, j, k, m, 1] + q5 * A5 [i, j, k, m, 2]$$

**END FOR**  
**END FOR**  
**END FOR**  
**END FOR**

---

The matrix A4 has to be now interpolated over 4 dimensions as explained in the next point.

- Interpolation over 4 dimensions can be now carried out as written in a pseudo code fragment in the following. Let's consider the matrix A4 as a four-dimensional array. The matrix A3 is the matrix for which the 4<sup>th</sup> dimension of A4 was interpolated.

---

**Pseudo code algorithm:** Interpolation 4D

---

**FOR** each element of first dim = i  
**FOR** each element of second dim = j  
**FOR** each element of third dim = k

$$A3 [i, j, k] = p4 * A4 [i, j, k, 1] + q4 * A4 [i, j, k, 2]$$

**END FOR**  
**END FOR**  
**END FOR**

---

The matrix A3 has to be now interpolated over 3 dimensions as explained in the next point.

- Interpolation over 3 dimensions can be now carried out as written in a pseudo code fragment in the following. Let's consider the matrix A3 as a three-dimensional array. The matrix A2 is the matrix for which the 3<sup>th</sup> dimension of A3 was interpolated.

---

**Pseudo code algorithm:** Interpolation 3D

---

**FOR** each element of first dim = i  
**FOR** each element of second dim = j

$$A2 [i, j] = p3 * A3 [i, j, 1] + q3 * A3 [i, j, 2]$$

**END FOR**  
**END FOR**

---

The matrix A2 has to be now interpolated over 2 dimensions as explained in the next point.

- Interpolation over 2 dimensions can be now carried out as written in a pseudo code fragment in the following. Let's consider the matrix A2 as a two-dimensional

array. The matrix A1 is a vector for which the 2<sup>nd</sup> dimension of A2 was interpolated.

---

**Pseudo code algorithm:** Interpolation 2D

---

**FOR** each element of first dim = i

$$A1 [i] = p2 * A2 [i, 1] + q2 * A2 [i, 2]$$

**END FOR**

---

The matrix A1 has to be now interpolated over 1 dimension as explained in the next point.

- Interpolation over 1 dimension can be now carried out as written in a pseudo code fragment in the following. Let's consider the matrix A1 as a vector. The matrix A0 is the interpolated value for which the dimension of A1 was interpolated.

---

**Pseudo code algorithm:** Interpolation 1D

---

$$A0 = p1 * A1 [1] + q1 * A1 [2]$$

---

### 2.3.2.1.1.3 Compute Partial Derivatives

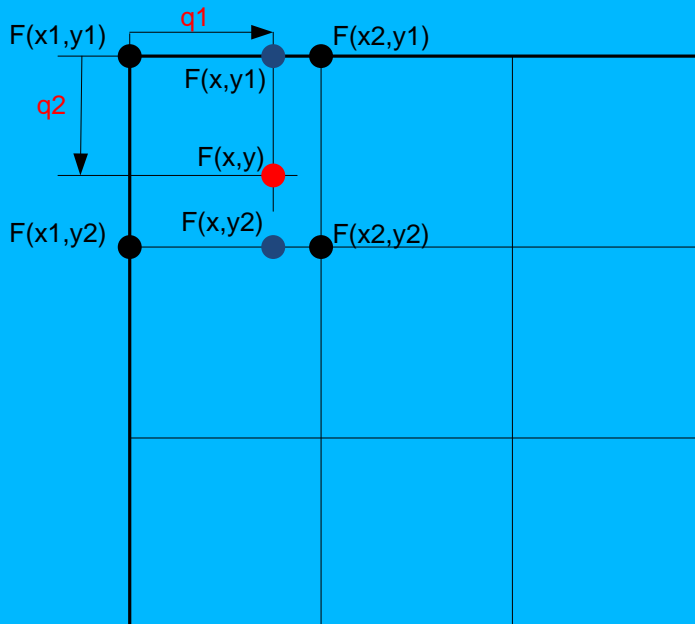


Figure 9 Pictorial depiction of LUT linear interpolation in both one and two dimensions.

This section is concerned with the numerical determination of the partial derivatives used to construct the Jacobian described used during the retrieval as described in section 3.4.2.3.

Partial derivatives in DCOMP are calculated in respect to  $\tau_c$  or  $r_e$  from 2D fields of cloud reflectance, transmission or spherical albedo. Let now  $F(x,y)$  be any one of the functions above with the two variables  $x = \tau_c$  and  $y = r_e$ . If we keep  $y$  constant with a value  $y_0$  and differentiate  $f$  with respect to variable  $x$ , we obtain what is called the partial derivative of  $F$  with respect to  $x$  which is denoted by  $\frac{\partial F(x, y_0)}{\partial x}$ . Similarly if we keep  $x$  constant with a value  $x_0$  and differentiate  $F$  with respect to the variable  $y$ , we obtain what is called the partial derivative of  $F(x,y)$  with respect to  $y$  which is denoted by  $\frac{\partial F(x_0, y)}{\partial y}$ . We can compute the partial derivatives of  $F$  referring to following:

$$\begin{aligned} F(x_1, y_0) &= p_2 F(x_1, y_1) + q_2 F(x_1, y_2) \\ F(x_2, y_0) &= p_2 F(x_2, y_1) + q_2 F(x_2, y_2) \\ \frac{\partial F(x, y_0)}{\partial x} &= \frac{F(x_2, y_0) - F(x_1, y_0)}{x_2 - x_1} \end{aligned} \quad (14)$$

Similarly for the derivatives in respect to  $y$ :

$$\begin{aligned} F(x_0, y_1) &= p_1 F(x_1, y_1) + q_1 F(x_2, y_1) \\ F(x_0, y_2) &= p_1 F(x_1, y_2) + q_1 F(x_2, y_2) \\ \frac{\partial F(x_0, y)}{\partial y} &= \frac{F(x_0, y_2) - F(x_0, y_1)}{y_2 - y_1} \end{aligned} \quad (15)$$

### 2.3.2.2 Atmospheric Correction

Atmospheric correction is needed to take into account any extinction processes in the atmospheric column. Table 8 summarizes all parameters in this section.

**Table 9 Parameters used in the section “Atmospheric Correction”**

Parameter	Symbol	Typical Value
Reflectance ( at top of atmosphere, top of cloud)	$R$ ( $R_{TOA}, R_{TOC}$ )	0.4

Reflectance backscattered to sensor	$R_{sc}$	0.1
Transmittance function (above, below cloud)	$T(T_{ac}, T_{bc})$	0.95
.. through water vapor including trace gases	$T_{h_2o}$	0.91
.. through ozone, aerosol, air molecules	$T_{o_3}, T_{aer}, T_r$	0.93
Local zenith angle, cosines of	$\theta, \mu$	34, 0.7
Solar zenith angle, cosines of	$\theta_0, \mu_0$	34, 0.7
Relative azimuth difference	$\Delta\varphi$	120
Optical depth for clouds, Rayleigh, aerosol	$\tau_c, \tau_r, \tau_{aer}$	12 0.03 0.05
Background optical depth for Rayleigh, aerosol	$\tau_{r,0}, \tau_{aer,0}$	0.044 0.1
Effective radius	$r_e$	10 $\mu m$
Rayleigh phase function	$P_r$	0.2
Scattering angle	$\zeta$	123
Cloud albedo	$A_c$	0.4
Spherical cloud albedo	$R_c^*$	0.1
Air mass factor	$AMF$	2.9
Asymmetry parameter	$g$	0.7
Single-scattering albedo	$\omega_0$	1
Surface pressure, cloud top pressure	$P_{sfc}, P_c$	540hPa 1013hPa
Water vapor mass	$u_{H_2O}$	0.17 dm
Ozone mass	$u_{O_3}$	382 Dobson

Atmospheric corrections will be carried out during the retrieval process at the pixel-level before the inversion process starts. A two-level atmospheric correction scheme is applied.

First, the atmospheric transmittance above the cloud is determined. The radiative transfer can influence the observed signal at TOA in different ways. Extinction of the direct photon path leads to a reduction in the reflectance at the TOA signal. Scattering processes, which deflect photons into the observed path, increase the signal. The reflectance at TOC can be calculated as:

$$R_{TOC} = \frac{R_{TOA} - R_{SCA}}{T_{ac}} \quad (16)$$

The values in Eq.(16)  $R_{TOC}$ ,  $R_{TOA}$  and  $R_{SCA}$  are the reflectance portions at TOC, TOA and the backscattered amount, respectively. The total transmission  $T_{ac}$  above the cloud ranges between 0 and 1.  $R_{TOC}$  is compared with the theoretical computed cloud reflectance  $R_C$  during the inversion process.

For the atmospheric layers below the cloud, the atmospheric transmission is considered by introducing a virtual surface albedo. The extinction below cloud expressed by  $T_{bc}$  can be treated as a reduction of the surface albedo:

$$A_{sfc,v} = A_{sfc} T_{bc} \quad (17)$$

The virtual surface albedo  $A_{sfc,v}$  substitutes the real surface albedo  $A_{sfc}$  for forward calculations in Eq.(12).

Non-negligible scattering processes occur only in the visible channel. Extinction is considered for scattering processes caused by air molecules (Rayleigh scattering) and aerosols and from absorption caused by water vapor, other trace gases, and ozone.

The transmission and backscattered reflection values under consideration of the relative amount of extinction in both channels are broken down as follows:

$$T_{ac,VIS} = T_r T_{aer} T_{o3} T_{h2o} \quad (18)$$

$$T_{ac,NIR} = T_{h2o} \quad (19)$$

We consider a backscattered signal  $R_{sca}$  only in the visible channel from Rayleigh scattering, so that

$$R_{sca,VIS} = R_{sca,r} \quad (20)$$

$$R_{sca,NIR} = 0 \quad (21)$$

The following subsections explain the individual parts of atmospheric correction in detail.

#### 2.3.2.2.1 Atmospheric Correction for Rayleigh scattering

Rayleigh scattering has a primary impact in the visible channel. Scattering in the near-infrared channel at 2.2  $\mu\text{m}$  is weak and negligible and is therefore ignored in the DCOMP algorithm. The potential error especially for thin clouds or high observing and solar angles reaches values from more than 10%. Figure 9 depicts the importance of Rayleigh correction for cloud optical depth retrieval.

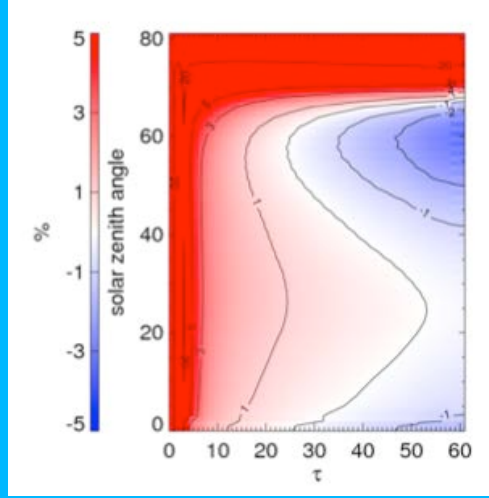


Figure 10 Potential error in percent if Rayleigh correction is not applied as a function of  $\tau_c$  and solar zenith angle. Observation angle is 43 degrees and effective radius is  $8 \mu m$ .

The correction scheme mainly follows the correction scheme by [Wang and King, 1997], which was also applied to MODIS processing. We consider the full atmospheric column of Rayleigh optical depth as  $\tau_{r,0} = 0.044$ . The resulting Rayleigh optical depth above the cloud is calculated by

$$\tau_r = \tau_{r,0} \left( \frac{p_c}{p_{sfc}} \right) \quad (22)$$

where  $p_c$  denotes the cloud top pressure provided by the ABI Cloud Height algorithm and  $p_{sfc}$  denotes the surface pressure and is provided by the NWP dataset.

It was assumed that the upward radiance at TOA can be broken down into four components by a single scattering assumption:

- (i) direct molecular scattering without reflection from the cloud;
- (ii) single scattering in the air toward the cloud followed by reflection from the cloud;
- (iii) as (ii), but vice versa; and
- (iv) direct reflection of the solar beam from the cloud.

[Wang and King, 1997] stated that under the single scattering assumption, the signal at the sensor  $R_{TOA}$  is composed of four parts by using cloud albedo  $A_c$ , the Rayleigh phase function  $P_r$ :

$$R^{(i)}(\tau_r, \theta, \theta_0, \Delta\phi) = \frac{\tau_r P_r(\theta, \theta_0, \Delta\phi)}{4\mu\mu_0} \quad (23)$$

$$R^{(ii)}(\tau_r, \tau_c, r_e, \theta, \theta_0) = \frac{\tau_r}{2\mu_0} A_c(\tau_c, r_e, \theta) e^{-\tau_r/\mu} \quad (24)$$

$$R^{(ii)}(\tau_r, \tau_c, r_e, \theta, \theta_0) = \frac{\tau_r}{2\mu} A_c(\tau_c, r_e, \theta_0) e^{-\tau_r/\mu_0} \quad (25)$$

$$R^{(iv)}(\tau_r, \tau_c, r_e, \theta, \theta_0, \Delta\phi) = R_{TOC}(\tau_c, r_e, \theta, \theta_0, \Delta\phi) e^{[-\tau_r, AMF]} \quad (26)$$

$$R_{TOA} = R^{(i)} + R^{(ii)} + R^{(iii)} + R^{(iv)} \quad (27)$$

where  $AMF = \frac{1}{\cos\theta} + \frac{1}{\cos\theta_0}$  is air mass factor. Note that all symbols are defined in Table 8.

The four parts are the direct scattering at an air molecule without reflection from the cloud ( $R^{(i)}$ ), a scattering first at an air molecule with a subsequent reflection at the cloud ( $R^{(ii)}$ ), the reflection first at the cloud top with a subsequent scattering event at an air molecule ( $R^{(iii)}$ ), and the direct reflection at the cloud top ( $R^{(iv)}$ )

We assume a Rayleigh optical depth for an atmospheric column from the surface to TOA for the visible channel of  $\tau_{r0} = 0.044$ . Rayleigh optical depth above the cloud are estimated by

$$\tau_r = \frac{p_c}{p_{sfc}} \tau_{r0} \quad (28)$$

where  $p_{sfc}$  and  $p_c$  are the surface pressure and the pressure at the cloud top, respectively. We use an NWP re-analysis surface pressure for  $p_{sfc}$  and ABI cloud top pressure for  $p_c$ . The Rayleigh phase function is expressed by

$$P_r(\theta, \theta_0, \Delta\phi) = \frac{3}{4} (1 + \cos\zeta(\theta, \theta_0, \Delta\phi))^2 \quad (29)$$

where  $\zeta(\theta, \theta_0, \Delta\phi)$  is the scattering angle.

The cloud albedo function  $A_c$  is given as pre-calculated LUTs as a function of  $\tau_c, r_e, \theta_0$ . Thus, the Rayleigh atmospheric correction should be a part of the optimization process for a perfect solution. However, the potential error is low and the computational cost would be immense if the Rayleigh correction would be a part of the inversion. Thus, to simplify the retrieval we approximate the effective radius  $r_e$  to be  $10\mu m$  for water clouds and approximately  $20\mu m$  for ice clouds. The residual problem turns to a 1D problem and the corresponding cloud optical depth can be found now by searching the minima difference between the observation in the visible channel and the LUT values for the visible channel for the chosen effective radius.

So, all needed parameters of equations (23) - (27) are given.

The term  $e^{-\tau_r, AMF}$  in Eq.(26) is the total two-way Rayleigh transmission function  $T_{ac}$  of the photon path on its way from the top of the atmosphere to the cloud surface and back to the sensor. Now we can use equations (23) to (27) to formulate a Rayleigh specific version of equation(16):

$$R_{TOC} = \frac{R_{TOA} - (R^{(i)} + R^{(ii)} + R^{(iii)})}{T_{ac}} \quad (30)$$

The values to include in equations (18) and (21) are as follows:

$$T_{r, VIS} = e^{-\tau_r, AMF} \quad (31)$$

$$T_{r,NIR} = 1. \quad (32)$$

$$R_{sca,VIS} = R^{(I)} + R^{(II)} + R^{(III)} \quad (33)$$

### 2.3.2.2.2 Atmospheric Correction for Aerosol Scattering Effects

For atmospheric correction of aerosols above clouds we assume a background aerosol optical depth of  $\tau_{aer,0} = 0.1$  with an asymmetry parameter  $g$  assumed to equal 0.6. The expression for the aerosol optical depth above a cloud takes into account the assumed vertical distribution of aerosol in the atmosphere with

$$\tau_{aer} = \left( \frac{p_c}{p_{sfc}} \right)^A \tau_{aer,0} \quad (34)$$

Forward scattering dominates the aerosol phase function of the aerosol. Thus, it is appropriate to substitute the optical depth by the scaled optical depth as:

$$\tau'_{aer} = \tau_{aer} (1 - \omega_0 g) \quad (35)$$

Background full-path aerosol parameters are summarized in Table 9.

**Table 10 Global settings for aerosol parameters**

Parameter	Symbol	Value
Aerosol optical depth	$\tau_{aer}$	0.1
Single-scattering albedo	$\omega_0$	0.9
Asymmetry	$g$	0.6

The relevant parameter for the correction scheme is:

$$T_{aer,VIS} = e^{-\tau'_{aer} AMF} \quad (36)$$

We assume transmission in the infrared channel as 1 and the backscattered portion as insignificant.

With the considerations for Rayleigh and aerosol atmospheric correction we can define an effective phase functions for scattering processes as:

$$P_{eff}(q) = \frac{w_{0,aer} t_{aer} P_{aer}(q) + t_{ray} P_{ray}(q)}{t_{tot}} \quad (37)$$

### 2.3.2.2.3 Atmospheric Corrections for Water Vapor Absorption and Trace Gases

To simplify the atmospheric corrections, the transmission of gas is parameterized as an analytical function of the effective absorber amount.

Water vapor mass above and below cloud is obtained from NWP water vapor profiles. The ACHA cloud top height is used for determining the cloud top level. The input profiles are functions of water vapor amount above the respective level  $w = f(z)$ :

$$u_{h_2o}^{AC}(cth) = w(cth) \quad (38)$$

The water vapor mass below cloud is calculated by the difference between the full column water vapor and the amount above the cloud top height as.

$$u_{h_2o}^{BC} = w(cth = 0) - u_{h_2o}^{AC} \quad (39)$$

In case of invalid NWP water profile data,  $u$  is set to a minimal value of 0, if this value becomes negative for corrupt data. Water vapor transmission is a function of the water vapor mass. MODTRAN simulations are used to find coefficients  $c_{0,1,2}$  which are applied to find the optical depth of water vapor according to:

$$\tau_{h_2o,\lambda} = c_{0,\lambda} + c_{1,\lambda}u_{h_2o} + c_{2,\lambda}u_{h_2o}^2 \quad (40)$$

where  $u_{h_2o}$  is water vapor column in mm column amount.

The transmission is now computed by:

$$T_{h_2o} = e^{-AMF \tau_{h_2o}} \quad (41)$$

where AMF is the relative air mass for both ways from the top of atmosphere and back,  $\tau_{H_2O,\lambda}$  is the optical depth of water vapor for a certain wavelength,  $c$  are coefficients retrieved by MODTRAN and  $W$  is the water vapor amount above the cloud.

**Table 11 Water vapor correction coefficients exemplarily for GOES-ABI**

	Ch1	Ch 3
$c_0$	3.73583E-4	-6.6015E-6
$c_1$	4.92151E-3	1.09070E-3

$$c_2 \quad \left| \begin{array}{l} -1.78257E-4 \\ -1.92701E-6 \end{array} \right.$$

**Table 12 Water vapor correction coefficients for SEVIRI**

	Ch 1	Ch 3
$c_0$	4.4758E-5	-7.1626E-5
$c_1$	2.6479E-2	-3.40936E-4
$c_2$	-7.13698E-5	-1.12104E-4

Table 10 and 11 include the coefficients for ABI and the proxy sensor.

Figure 10 shows the transmission for AMF =1 as a function of the absorber mass for both channels.

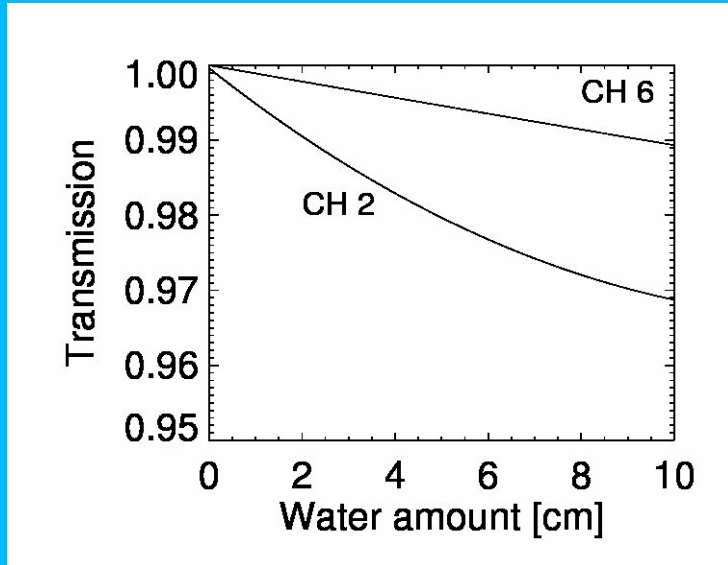


**Figure 11 Water vapor transmission as a function of absorber amount.**

#### 2.3.2.2.4 Ozone

Similarly, ozone transmission is calculated as:

$$T_{o_3} = e^{-AMF \tau_{o_3}} \quad (42)$$

where  $\tau_{o_3}$  is the ozone optical thickness;

$$\tau_{o_3} = c_0^{o_3} + c_1^{o_3} u_{o_3} + c_2^{o_3} u_{o_3}^2 \quad (43)$$

The value  $u_{o_3}$  is the ozone absorber mass in Dobson units. The coefficients were computed by MODTRAN simulations. Values are  $c_0^{o_3} = 0.000566454$  ,  $c_1^{o_3} = 8.25224e-05$  and  $c_2^{o_3} = 1.94007e-08$  . Ozone transmission are ignored in the near infra-red channel.

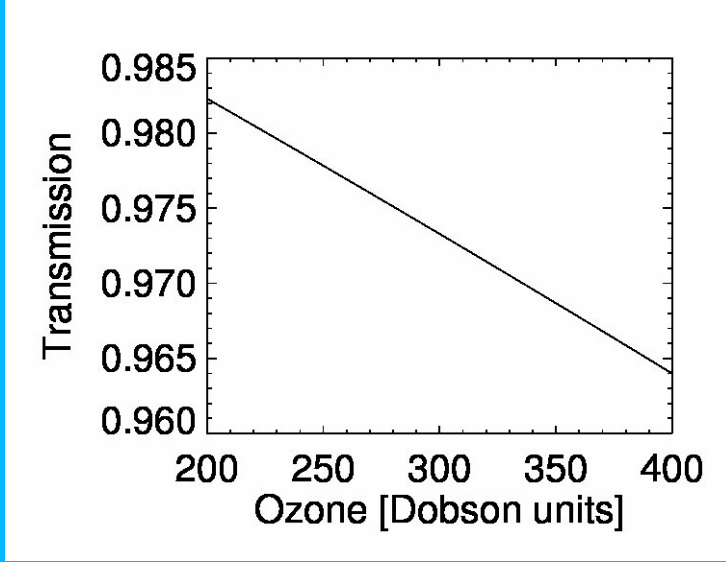


Figure 12 Ozone transmission as a function of absorber amount

### 2.3.2.3 Optimal Estimation Inversion Technique

Using optimal estimation (OE) proved to be a fast and accurate inversion technique for deriving properties from satellite measurements [Rodgers, 2000] . This OE-algorithm aims to minimize a cost-function accounting for measurement errors, and prior knowledge given by simple assumptions.

The covariance error matrix of the state  $x$  is calculated by

$$\mathbf{S}_x = (\mathbf{S}_a^{-1} + \mathbf{K}^T \mathbf{S}_y^{-1} \mathbf{K})^{-1} \quad (44)$$

where  $y$  is the observation vector,  $x$  the state vector,  $x_a$  the a-priori state vector,  $F$  the forward model operator,  $K$  the Kernel and  $S_a$  and  $S_y$  the observation and background error covariance matrixes. The setting of the prior knowledge parameters  $x_a$ ,  $S_a$  and  $S_y$  are explained in the next section. The state vector  $x$  for the next iteration step  $i+1$  is calculated after a row of iterative steps according to

$$x_{i+1} = x_i + \delta x \quad (45)$$

$$\delta x = \mathbf{S}_x \left( \mathbf{K}^T \mathbf{S}_y^{-1} (y - F(x_i)) + \mathbf{S}_a^{-1} (x_a - x) \right) \quad (46)$$

Starting from a first guess that is typically the a priori value  $\mathbf{x}_a$ , the iteration is performed until a convergence criterion is fulfilled or the number of iterations exceeds a maximum threshold. The convergence test in DCOMP is based on the size of the iteration step in the state space. The retrieval iterations are conducted until the following criterion is met:

$$d_i^2(\mathbf{x}_i - \mathbf{x}_{i+1}) = (\mathbf{x}_i - \mathbf{x}_{i+1})^T \mathbf{S}_x^{-1} (\mathbf{x}_i - \mathbf{x}_{i+1}) \leq \frac{p}{2} \quad (47)$$

where  $p$  is the number of elements of  $\mathbf{x}$  ( $p = 2$ ).

In DCOMP the  $\mathbf{y}$  and  $\mathbf{x}$  vectors are defined as follows.

$$\mathbf{x} = \begin{pmatrix} \tau \\ r_e \end{pmatrix} \quad (48)$$

$$\mathbf{y} = \begin{pmatrix} R_{VIS} \\ R_{IR} \end{pmatrix} \quad (49)$$

The Kernel matrix  $\mathbf{K}$  contains the partial derivatives of each element of  $F(\mathbf{x})$  in respect to each element of  $\mathbf{x}$ .

$$\mathbf{K} = \begin{pmatrix} \frac{\partial R^{ch2}}{\partial \tau} & \frac{\partial R^{ch2}}{\partial r_e} \\ \frac{\partial R^{ch6}}{\partial \tau} & \frac{\partial R^{ch6}}{\partial r_e} \end{pmatrix} \quad (50)$$

The forward operator which accounts for the surface is calculated by:

$$\mathbf{F}(\mathbf{x}) = R_c(\mathbf{x}, \theta, \theta_0, \Delta\varphi) + \frac{A_{sfc}}{1 - A_{sfc} R_c^*(\mathbf{x})} T(\mathbf{x}, \theta) T(\mathbf{x}, \theta_0) \quad (51)$$

The cloud reflectance  $R_c$ , spherical albedo  $R_c^*$  and the transmission  $T$  are determined from the LUTs. The surface albedo is given by the MODIS white sky albedo ancillary dataset. The individual components of  $\mathbf{F}(\mathbf{x})$  are:

$$R^{ch2} = R_c^{ch2}(\mathbf{x}, \theta, \theta_0, \Delta\varphi) + \frac{A_{sfc}^{ch2}}{1 - A_{sfc}^{ch2} R_c^{*,ch2}(\mathbf{x})} T^{ch2}(\mathbf{x}, \theta) T^{ch2}(\mathbf{x}, \theta_0) \quad (52)$$

$$R^{ch6} = R_c^{ch6}(\mathbf{x}, \theta, \theta_0, \Delta\varphi) + \frac{A_{sfc}^{ch6}}{1 - A_{sfc}^{ch6} R_c^{*,ch6}(\mathbf{x})} T^{ch6}(\mathbf{x}, \theta) T^{ch6}(\mathbf{x}, \theta_0) \quad (53)$$

To simplify the subsequent equations we substitute the second term of Eq. (52) with:

$$D_{sfc}^k = \frac{A_{sfc}^k}{1 - A_{sfc}^k R_c^{*,k}(\mathbf{x})} \quad (54)$$

The components of  $\mathbf{K}$  are derivatives of each forward model with respect to the components of the state vector and are calculated by:

$$\begin{aligned} \frac{\partial R^k}{\partial \tau} = & \\ & \frac{\partial R_c^k}{\partial \tau} + D_{sfc}^{ch6}(\mathbf{x}, \theta) \frac{\partial T^k(\mathbf{x}, \theta_0)}{\partial \tau} + D_{sfc} \frac{\partial T^k(\mathbf{x}, \theta)}{\partial \tau} T^k(\mathbf{x}, \theta_0) + \\ & \frac{\partial D_{sfc}}{\partial \tau} T^{ch6}(\mathbf{x}, \theta) T^k(\mathbf{x}, \theta_0) \end{aligned} \quad (55)$$

where k denotes the channel number 2 or 6 and derivatives of  $D_{sfc}$  are calculated by:

$$\frac{\partial D_{sfc}^k}{\partial \tau} = \frac{A_{sfc}^k A_{sfc}^k \frac{\partial R_c^{*,k}}{\partial \tau}}{(1 - A_{sfc}^k R_c^{*,k})^2} \quad (56)$$

Similar for the derivative to the effective radius:

$$\begin{aligned} \frac{\partial R^k}{\partial r_e} = & \\ & \frac{\partial R_c^k}{\partial r_e} + D_{sfc}^k T^k(\mathbf{x}, \theta) \frac{\partial T^k(\mathbf{x}, \theta_0)}{\partial r_e} + D_{sfc}^k \frac{\partial T^k(\mathbf{x}, \theta)}{\partial r_e} T^k(\mathbf{x}, \theta_0) + \\ & \frac{\partial D_{sfc}^k}{\partial r_e} T^k(\mathbf{x}, \theta) T^k(\mathbf{x}, \theta_0) \end{aligned} \quad (57)$$

with

$$\frac{\partial D_{sfc}^k}{\partial r_e} = \frac{A_{sfc}^k A_{sfc}^k \frac{\partial R_c^{*,k}}{\partial r_e}}{(1 - A_{sfc}^k R_c^{*,k})^2} \quad (58)$$

The maximum iteration number is set to 22. It can be shown that for the bulk of the pixels, the algorithm converges after 5-8 iterations. If the inversion loop exceeds iteration number of 20, it is very unlikely that a valid result is achievable.

#### 2.3.2.4 Estimation of Prior Values and their Uncertainty

The proper implementation of DCOMP requires meaningful estimates of a priori values housed in  $\mathbf{x}_a$  and their uncertainties housed in  $\mathbf{S}_a$ . For DCOMP, we assume  $\mathbf{S}_a$  is a diagonal matrix with each element assumed to be the variance of each element of  $\mathbf{x}_a$  as illustrated below:

$$S_a = \begin{pmatrix} \sigma_{\tau,ap}^2 & 0 \\ 0 & \sigma_{r_e,ap}^2 \end{pmatrix} \quad (59)$$

Since almost all estimates of COD and CPS from other algorithms are based on similar approaches, there is no robust a priori for these cloud parameters. In general, it is assumed that water clouds have a maxima effective radius size of up to 30 microns with an average of about 10 microns. Ice particles may have effective radii of up to 100 microns with a higher average. Optical depth is directly related to the extinction by scattering in a conservative wavelength. Consequently, we selected an a priori value that is related to the reflectance in the visible channel (ABI channel 2) and the a priori value of the effective radius. We search for the point of the iso-line of the a priori effective radius, where the observed reflectance in the visible channel is true, and take the corresponding optical depth as the a priori value.

According to the findings of several publications, we set the following a priori values for water:

$$\mathbf{x}_{ap} = \begin{pmatrix} \tau_{ap} \\ r_{e,ap} \end{pmatrix} = \begin{pmatrix} f(10, R_{CH2}) \\ 10^1 \mu m \end{pmatrix} \quad (60)$$

and for ice:

$$\mathbf{x}_{ap} = \begin{pmatrix} \tau_{ap} \\ r_{e,ap} \end{pmatrix} = \begin{pmatrix} f(10^{1.3} \mu m, R_{CH2}) \\ 10^{1.3} \mu m \end{pmatrix} \quad (61)$$

The uncertainty of these assumptions is high. Thus, we set the values  $\sigma_{\tau,ap}$  and  $\sigma_{r_e,ap}$  to 0.2 or the a priori value of  $\tau$ , and 0.5 for water and 0.75 for ice.

### 2.3.2.5 Estimation of Forward Model Uncertainty

This section describes the estimation of the elements of  $\mathbf{S}_y$  which contain the uncertainty of the observation vector  $\mathbf{y}$  as a variance of the forward model estimates. As was the case with  $\mathbf{S}_a$ ,  $\mathbf{S}_y$  is assumed be a diagonal matrix.

Assumed to be diagonal,  $\mathbf{S}_y$  can be expressed as follows.

$$S_y = \begin{pmatrix} \sigma_{CH2,ap}^2 & 0 \\ 0 & \sigma_{CH6,ap}^2 \end{pmatrix} \quad (62)$$

The variance terms are computed by summing up three components:

$$\sigma = \sigma_{OFF} + R^k (\sigma_{clb} + \sigma_{fm} + \sigma_{pp} \sigma_{hetero}) \quad (63)$$

The first component gives an offset as a bottom value for the assumed error. The sum of calibration error  $\sigma_{clb}$ , forward model error  $\sigma_{fm}$  and the plan-parallel error  $\sigma_{pp}$  multiplied by a

measure of spatial heterogeneity  $\sigma_{hetero}$  is weighted by the measured reflectance  $R^k$  of the individual channels  $k$ . The last term can be seen as an estimate of the error, which would occur if the plan-parallel assumption fails. We assume that this is particular uncertain in case of low spatial homogeneity.

If the snow mask from the framework detects snow surfaces, we will give the observations in the visible channel very low trust. This fact is reflected in a high value for  $\sigma$  in the visible channel.

**Table 13 The error estimated in forward model uncertainty in DCOMP**

		Channel 1	Channel 3
Calibration error	$\sigma_{clb}$	0.05	0.05
Forward model error water	$\sigma_{fm}$	0.01	0.01
Forward model error ice	$\sigma_{fm}$	0.03	0.03
Plan parallel error	$\sigma_{pp}$	0.1	0.1
Offset value	$\sigma_{off}$	0.02	0.02
Snow exception	$\sigma_{snow}$	1000.	

## 2.4 Algorithm Product Output

### 2.4.1 Output

The data product includes two float-typed datasets for cloud optical depth and cloud effective radius, which are passed through the processing system. The product data file type is determined by the software environment, and is for CLAVR-x and GEOCAT the HDF-4 scientific formatted file type.

Note, that an output for each pixel is either liquid water path or ice water path.

**Table 14 Algorithm output**

Name	Type	Description	Dimension	Unit
COD	output	Cloud optical depth	grid (xsize, ysize)	unitless
REF	output	Cloud effective radius	grid (xsize, ysize)	$\mu m$
CODU	output	Cloud optical depth uncertainty	grid (xsize, ysize)	unitless
REFU	output	Cloud effective radius uncertainty	grid (xsize, ysize)	$\mu m$
LWP	output	Liquid water path	grid (xsize, ysize)	g/m <sup>2</sup>
IWP	output	Ice water path	grid (xsize, ysize)	g/m <sup>2</sup>
QC flags	output	Quality control flags for each pixel	grid (xsize, ysize)	

### 2.4.2 Quality Flags

In addition to the algorithm output, a pixel level quality flag will be assigned. Since all products are generated in parallel, we set one single level of quality flags for DCOMP instead of one quality for each product. The possible values are as follows:

**Table 15 Quality Flags in DCOMP output**

	Bit	Description	When to apply
DCOMP_PRCS_FLAG	00000	0 - not processed 1- processed	0 - not processed 1- processed
DCOMP_QF_COD_VALID	1	0 –Valid retrieval 1- not valid	If Q1/B0 EQ ‘1’
DCOMP_QF_REF_VALID	2	0 –Valid retrieval 1- not valid	If Q1/B0 EQ ‘1’
DCOMP_QF_COD_DEGRADED <sup>1</sup>	3	0 –no 1- degraded	If Q1/B0 EQ ‘1’
DCOMP_QF_REF_DEGRADED <sup>2</sup>	4	0 –no 1- degraded	If Q1/B0 EQ ‘1’
DCOMP_QF_CONVERGENCY	5	0 – convergent 1 - not	If Q1/B0 EQ ‘1’
DCOMP_QF_GLINT	6	0 – no glint 1- glint	If Q1/B0 EQ ‘1’

<sup>1</sup> Reasons for COD degradation are set in DCOMP\_INFO flag. Possible reasons for COD are snow, sea-ice, twilight and thick cloud saturation.

<sup>2</sup> Reasons for REF degradation are set in DCOMP\_INFO flag. Possible reasons for REF degradation are snow, sea-ice, twilight.

Bits 1 to 6 are only to be applied if DCOMP\_PRDS\_LAG is set to “true”.

### 2.4.3 Processing Information Flag

In addition to the algorithm output and quality flags, processing information is output for each pixel. Table 16 lists the bitwise information.

**Table 16 Processing Information Flags in DCOMP**

	Bit	Description	When to apply
DCOMP_INFO_LAND_SEA	0	0 –Land 1- Ocean	
DCOMP_INFO_DAY_NIGHT	1	0 –Day 1-Night	
DCOMP_INFO_TWILIGHT	2	0- no 1- solar angle between 65 and 82	
DCOMP_INFO_SNOW	3	0 – no snow 1 -snow	
DCOMP_INFO_SEA_ICE	4	0 – no sea ice 1- sea ice	
DCOMP_INFO_PHASE	5	0 - water 1-ice	If QF1/B0 EQ

			'1'
DCOMP_INFO_THICK_CLOUD <sup>1</sup>	6	0 - no 1 - yes	If QF1/B0 EQ '1'
DCOMP_INFO_THIN_CLOUD <sup>2</sup>	7	0 - no 1 - yes	If QF1/B0 EQ '1'

<sup>1</sup> Thick cloud retrieval set COD to upper bound (160). The COD Quality is degraded. REF quality is good.

<sup>2</sup> Thin cloud retrieval set REF to a-priori value. The REF retrieval output is not valid. COD quality is good.

## 2.4.4 Metadata

The output files will include the following metadata:

- Day/Night flag
- Mean, Min, Max and standard deviation of cloud optical depth
- Mean, Min, Max and standard deviation of cloud particle size
- Number of QA flag values
- For each QA flag value, the following information is required:
  - Number of retrievals with the QA flag value
  - Definition of QA flag
- Total number of detected cloud pixels
- Terminator mark or determination

## 2.5 Performance Estimates

### 2.5.1 Test Data Sets and Output

As described above, most current sensors can be used as test data.

#### 2.5.1.1 Example for geostationary sensor: SEVIRI

DCOMP can be run on all relevant geostationary sensors, such as SEVIRI, GOES series, AHI, FY2. SEVIRI provides 16 spectral channels with an approx. spatial resolution of 4km every 15 minutes. Figure 13 shows a true color image for SEVIRI scene of 1 August 2006 1300 UTC.



**Figure 13 Full disk true color image from SEVIRI 13UTC on 1 August 2006.**

Except for the exact channel settings, all components of the algorithm system, such as radiative transfer model, LUT design and inversion technique are identical to every other sensor. Figure 14 shows DCOMP products from SEVIRI observations for 13:00 UTC on 1 August 2006.. The images in Figure 14 illustrate the DCOMP products Cloud optical depth, Cloud Particle Size, Liquid Water Path and Ice Water Path. These images correspond to 13 Z on 1 August 2006 and correspond to the RGB image above. This day and scene was chosen since it was also used in a EUMETSAT SEVIRI cloud product comparison workshop in Locarno/Switzerland.

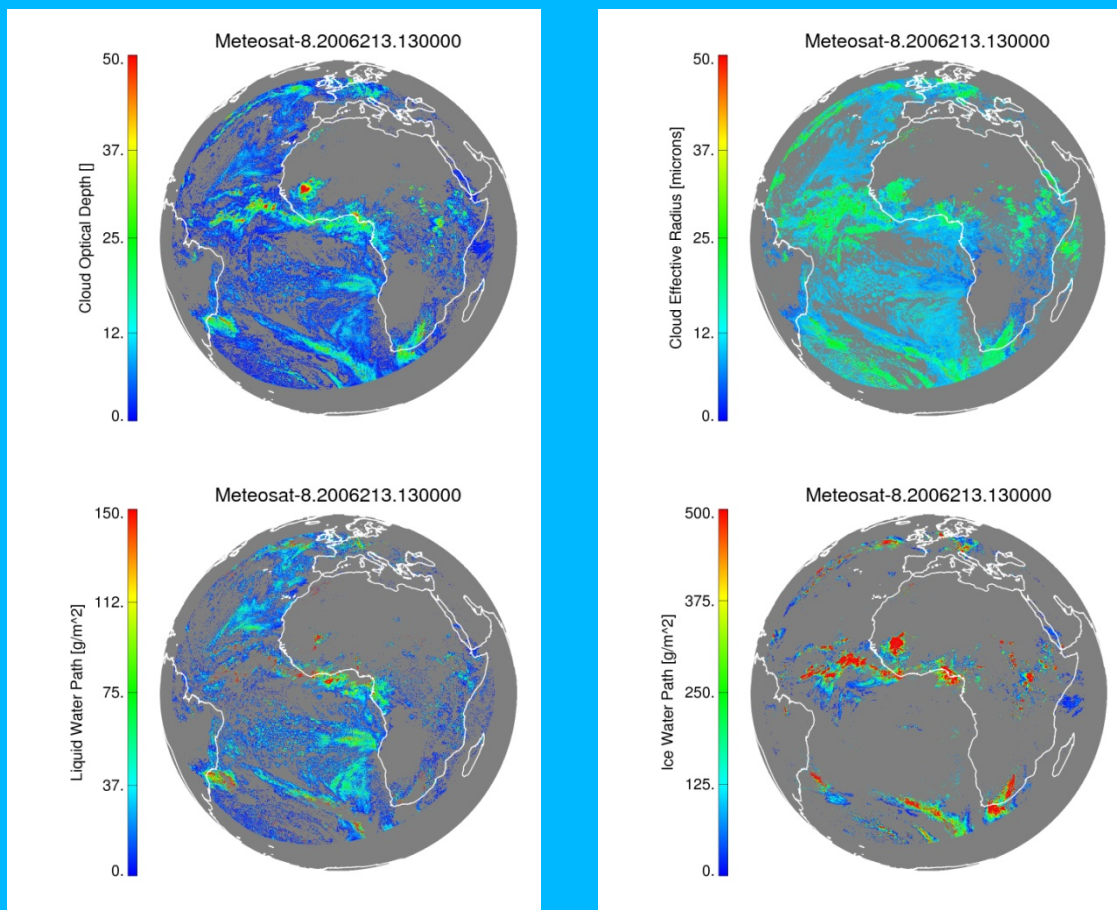


**Figure 14** Results of the retrieval for 1 August 2006 13:00UTC for SEVIRI. Upper panel shows optical depth (left) and effective radius (right). Lower panel shows liquid water path (left) and ice water path (right).

### 2.5.1.2 Example for polar-orbiting data: VIIRS/NPP Suomi

DCOMP can be processed on the several polar-orbiting sensors (see section 1). We show here exemplarily results for VIIRS on Suomi NPP on 2013 Day 127 1240 UTC.

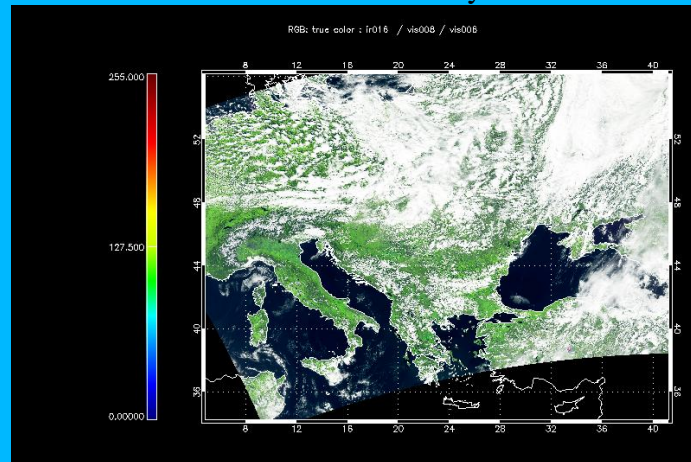


**Figure 15** True color image for VIIRS/NPP scene.

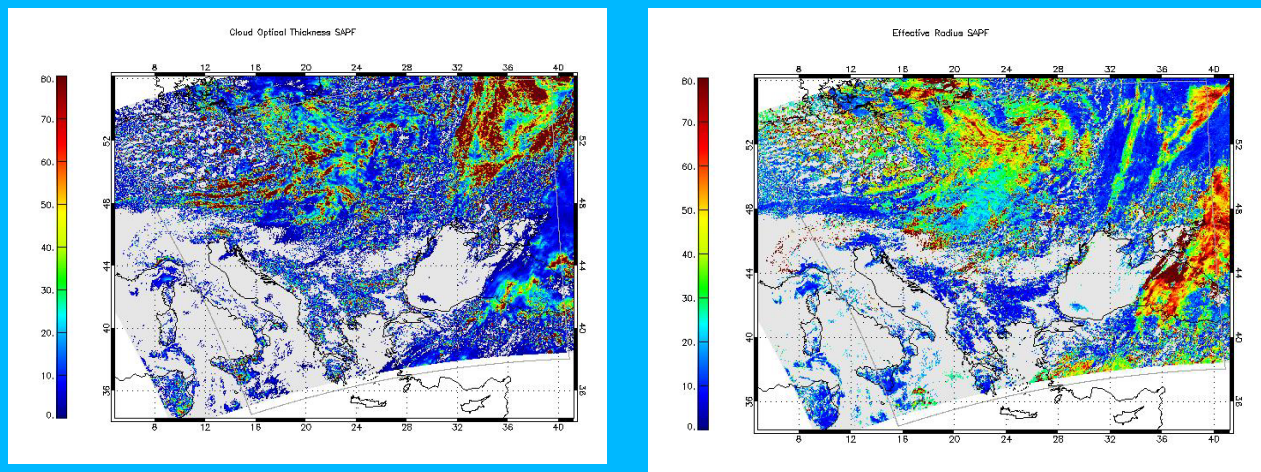


**Figure 16** DCOMP output COD (left) and CPS (right) for VIIRS/NPP

### 2.5.1.3 DCOMP and the PATMOS-x AVHRR climate data set

DCOMP is a part of the climate data set PATMOS-x, which spans more than 30 years of AVHRR cloud observations on NOAA satellites. The generation of PATMOS-x level2b data is extensively described in Heidinger et al. 2013.

Cloud products are stored in a “level-2b” data format, which samples the cloud products in a regular 0.1 x 0.1 degree longitude/latitude grid. The sampling does not include any averaging, so

that the algorithm space is conserved. Result is a handy and flexible climate data set, which is makes it easy to investigate any climate questions concerning clouds and atmospheric parameters.

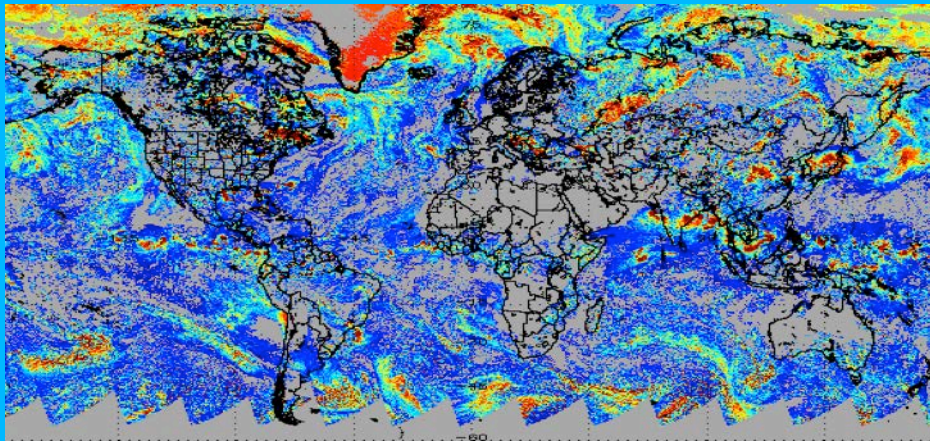


Figure 17 DCOMP Cloud Optical Thickness for one day of PATMOS-x level2b data from NOAA-18.

While the PATMOS-x data set was originally designed for NOAA satellite series, similar data sets are also generated for other appropriate sensors, such as MODIS, GOES and VIIRS. We use inter-comparison between multiple sensors as an additional evaluation of the performance and quality of DCOMP.

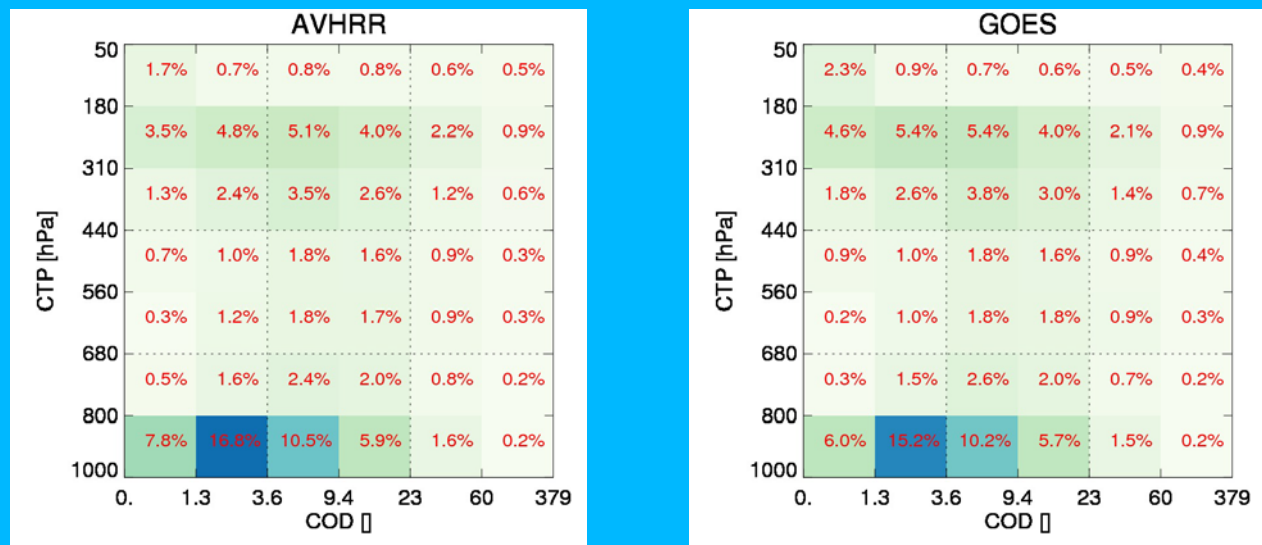
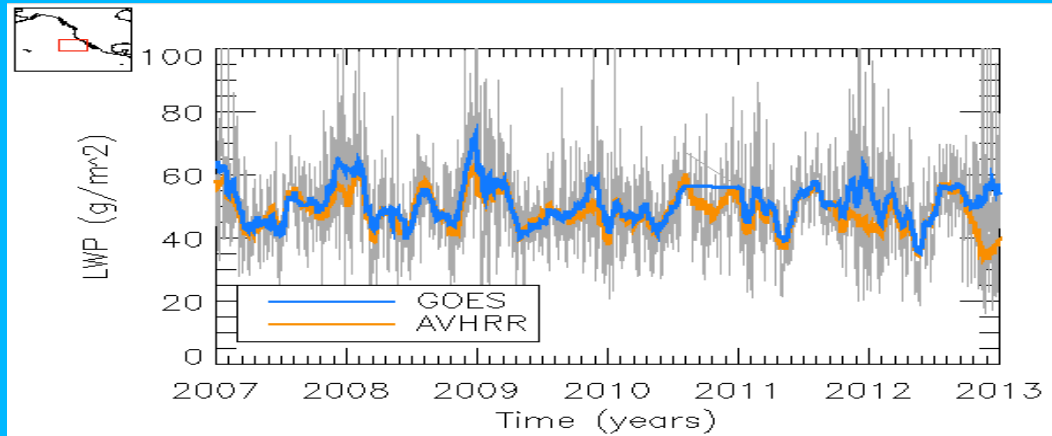


Figure 18 Comparison of level2b data from the AVHRR PATMOS-x data set ( left) and a similar level-2b data set derived by GOES-EAST satellite

Figure 24 shows as an example the distribution of COD as a function of the derived cloud top pressure for one day of level2b data over the continental USA.



**Figure 19** Time series of Liquid water path from DCOMP results in PATMOS-x data set in comparison to GOES-West results.

Figure 17 shows a time series of liquid water path derived by DCOMP over a part of Pacific Ocean off the Californian coast.

## 2.5.2 Sensor Effects

The signal-to-noise relation taken from technical documents are considered in input uncertainty and will be propagated to output uncertainty.

## 2.6 Practical considerations

### 2.6.1 Numerical Computation Considerations

The algorithm is currently able to be implemented into NOAA/NESDIS framework and uses its numerical routines for processing. For SEVIRI proxy data (several data fields of 3712 x 3712 float elements) we run the algorithm on a 200 scan-line basis to avoid memory issues. The inversion process requires a large number (up to 50 times per pixel) of search events in look-up-tables. We explicitly paid attention on memory budget to speed up the code. The algorithm runs for a full SEVIRI scene in under five minutes.

### 2.6.2 Programming and Procedural Considerations

All code is written in the FORTRAN 90 programming language. It consists of one file with a FORTRAN *module* with several subroutines. An *include* file declares variable names of the software environment. It was tested to work in the framework environment.

The core algorithm is a pixel-by-pixel algorithm. The program interacts with the environment through data access subroutines. This program architecture makes it easy to run it in other ambient systems as well.

All input parameters that come from an external source are tested whether they fall in an expected and allowable range. All routine input parameters are also checked even if they come from another internal routine. Assertion code is included in each subroutine.

Global values were avoided as much as possible. Access to all variables from all subroutines is done by data access routine. We use pointer variables for output and several other parameters. Within the program we took care that all pointers' memory is freed.

### **2.6.3 Quality Assessment and Diagnostics**

The following flags will be produced:

- Missing / No data
- Cloud-free
- Cloudy, but no convergence
- High value of cost function

### **2.6.4 Exception Handling**

The algorithm checks the validity of each channel. The DCOMP algorithm also expects the main processing system to flag any pixels with missing geo-location or viewing geometry information.

The algorithm does check for conditions where the algorithm cannot be performed. These conditions include saturated channels or missing RTM values. In these cases, the appropriate flag is set to indicate that no value was produced for that pixel.

The following exception handlings are applied:

- If the MODIS surface albedo is missing, we use a default value (for land surfaces) of 0.15 instead.
- If NWP data are missing, we will use a default water vapor profile instead. This option is not currently implemented.

## **2.7 Algorithm Validation**

Cloud optical parameters, in particular optical depth, are difficult to validate. Unlike other cloud parameters, cloud optical thickness is a radiative property. Thus, it is not possible to validate optical depth directly from in-situ measurements without making assumptions about the scattering of cloud particles.

However, a first sanity check is the comparison with retrievals existing in the scientific community.

To estimate the precision and accuracy of DCOMP products, MODIS data from AQUA and TERRA satellite are used. To validate liquid water path, observations of passive microwave sensor AMSR-E are used. Inter-comparisons with SEVIRI products of other research groups is an additional quality check.

Validating DCOMP products has been performed in several steps:

- Direct comparison with MODIS products. These retrievals use the same retrieval principle and therefore can be considered only as a sanity check.
- For liquid water clouds, the use of passive microwave retrievals from AMSR-E and SSM/I may help to validate the liquid water path.
- A-TRAIN measurements can help to identify aerosol layers that possibly falsify the results.

### 2.7.1 Inter-comparison with Products of Other Research Groups

Validation strategies for optical parameters are rare. Therefore inter-comparison to other group's products are important consistency checks for newly introduced algorithms. The GOES ABI algorithm was compared with its SEVIRI counterpart at the EUMETSAT workshop in Ascona, Switzerland in February 2009. Participants at this workshop were from 16 different institutions from Europe and North America. The comparison was a strict pixel-base 1:1 comparison for all cloud products. In this document, we only show a small subset of the workshop results.

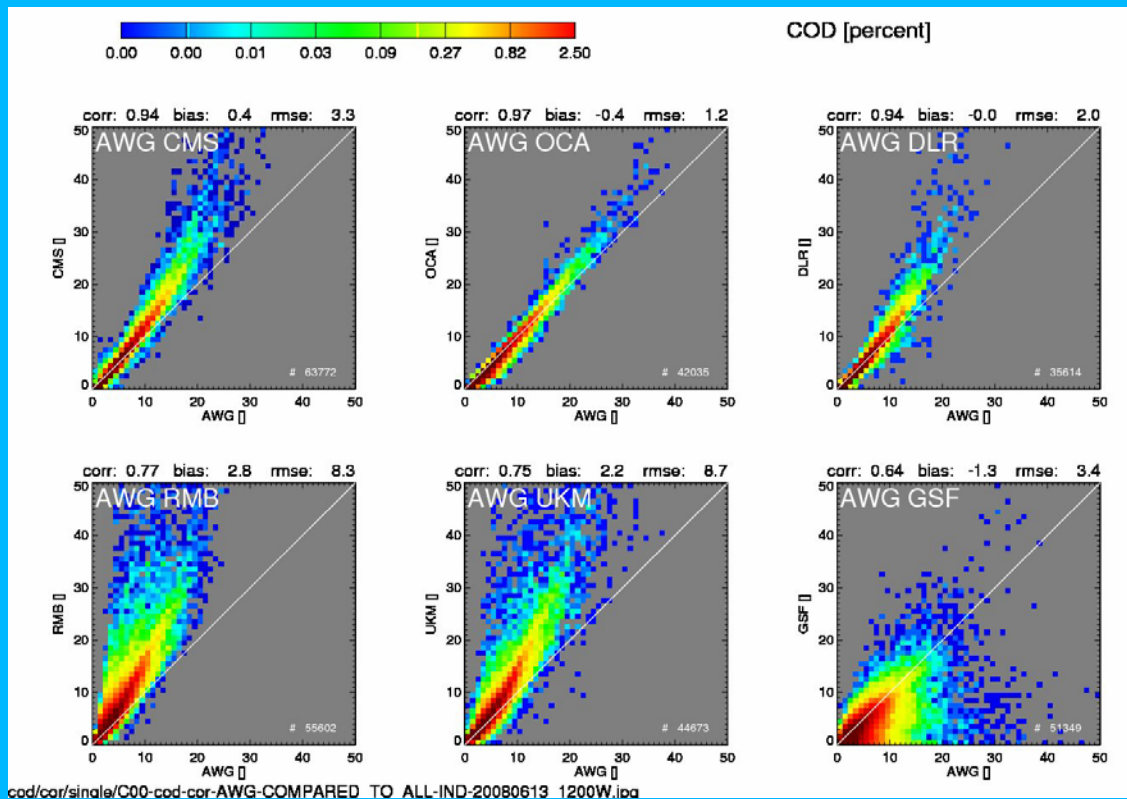


Figure 20 Comparison of DCOMP-COD for liquid water clouds algorithm (AWG) to six other groups.

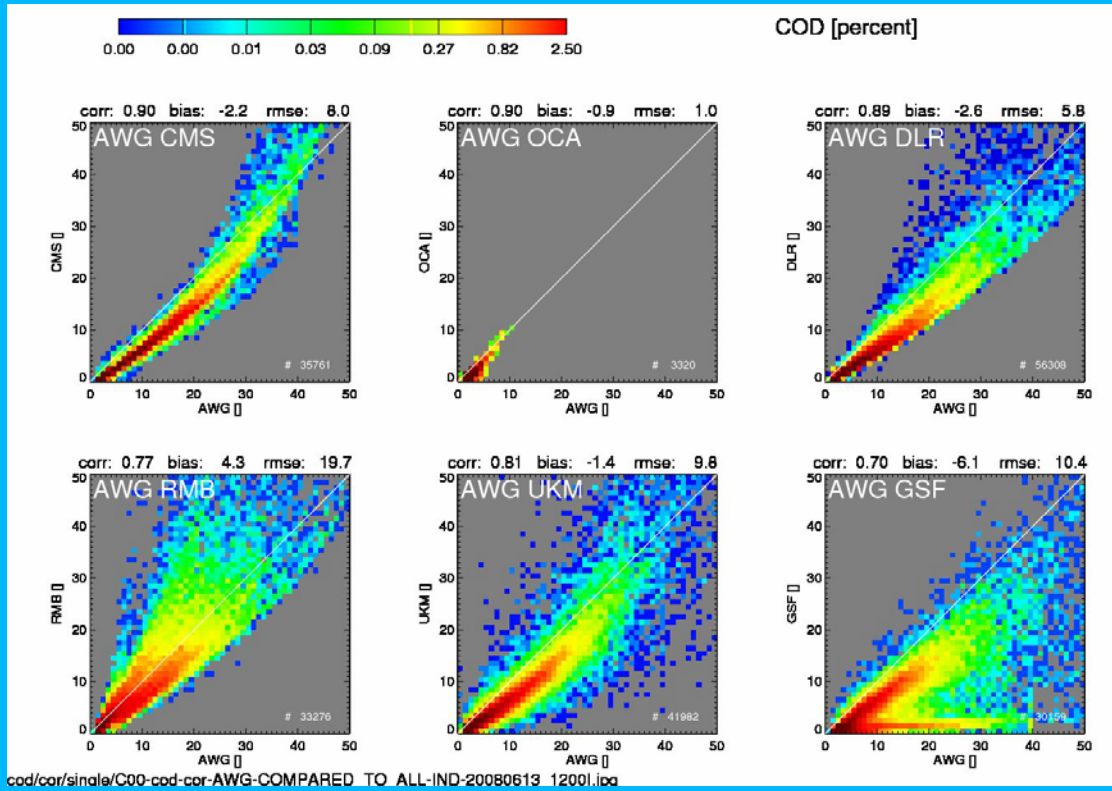


Figure 21 Comparison of DCOMP-COD Ice phase with six other groups.

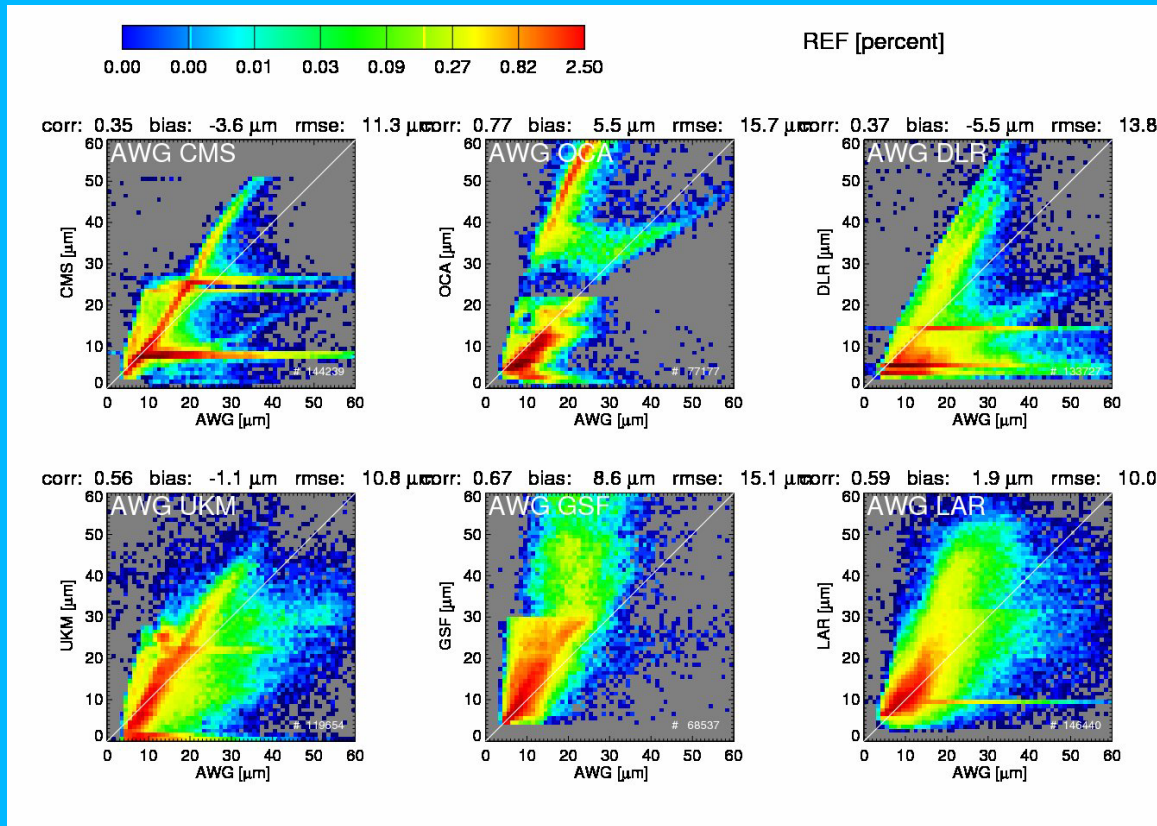


Figure 22 Comparison of DCOMP-REF all phases with six other groups.

Figures 14, 15 and 16 show the results of the comparison. The acronym “AWG” (“Algorithm Working Group”) denotes the DCOMP algorithm. In all sub-images the DCOMP algorithm represents the x-axis of the 2D histograms. The other products are from EUMETSAT groups (CMS, OCA), the German Aerospace Center (DLR), the U.K. Met Office (UKM), Goddard Space Flight Center (GSFC) and from NASA Langley Research Center (LARC). These are not official products and might be also in a test phase.

Figure 12 summarizes the results for COD water retrieval. DCOMP shows excellent agreement with most other algorithms.

Figure 16 shows the all-phase results for Cloud Particle Size. In contrary to some other groups, DCOMP does not show peaks in the histograms. Underestimating of a-priori error may cause this potential artifact in non-AWG retrievals.

## 2.7.2 Comparison with MODIS, AMSR-E along a CloudSat Track

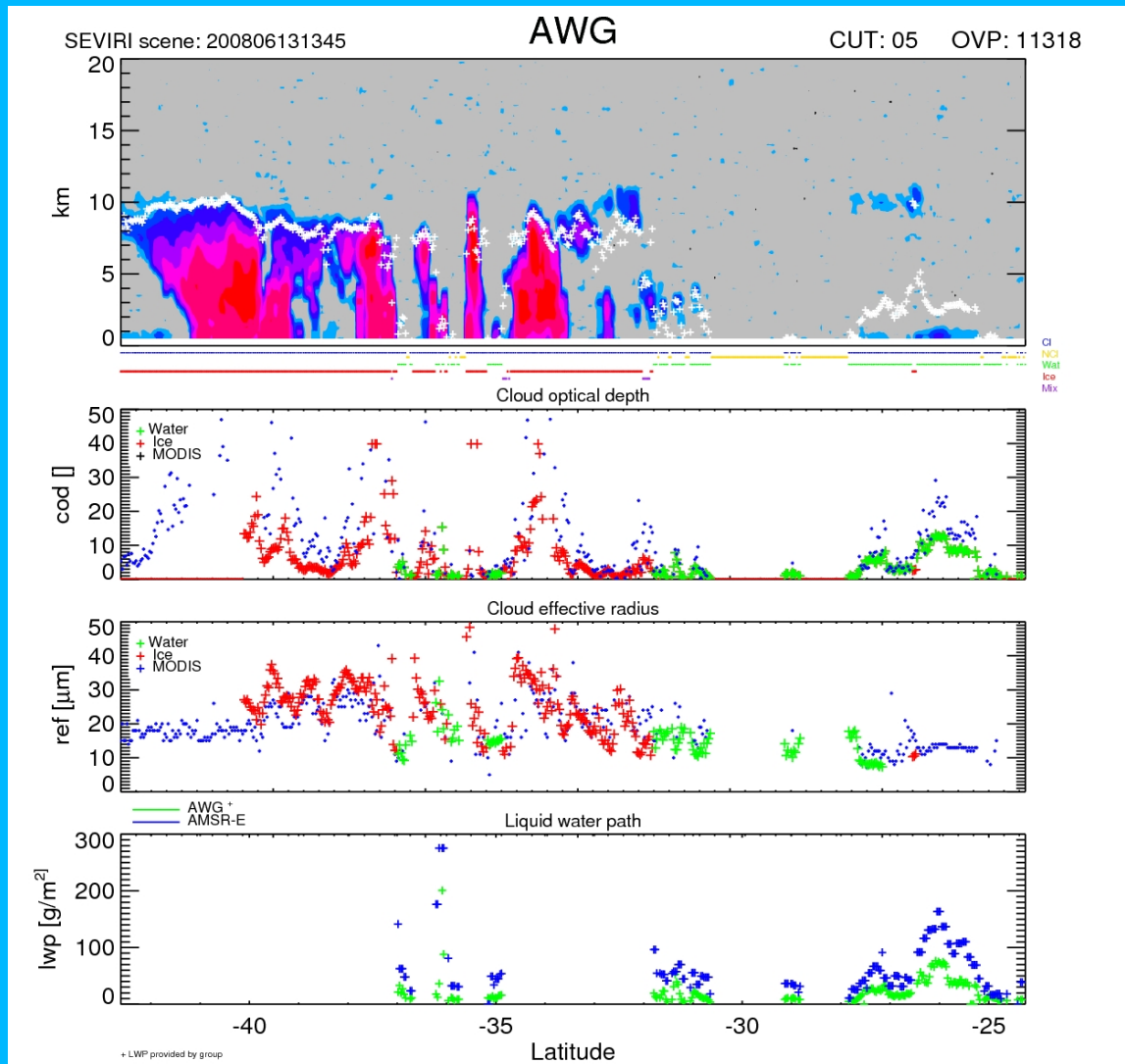


**Figure 23** Integrative comparison of ABI products. Upper panel shows CloudSat radar reflectivities with ABI cloud height (white crosses). Second panel shows comparison of DCOMP cloud optical depth of ice (red) and liquid water (green) with MODIS. Third panel shows same, but for effective radius. Bottom panel illustrates comparison of DCOMP liquid water path with AMSR-E.

The vertical profiles of radar reflectivity by CloudSat give a good opportunity to see in which situations the algorithm performs well and in which situations the algorithm has its weaknesses. In the upper panel of Figure 15 the CloudSat reflectance is shown with the result of the ABI Cloud Height product. The Cloud height performs well for thicker clouds but performs poorly with multi-layer clouds at around 26S latitude. This may also impacts DCOMP because it uses the ABI cloud height for atmospheric correction.

The other three panels are DCOMP product comparison with MODIS (image 2 and 3) and AMSR-E (4). Again, MODIS comparison does not represent a real validation, since it is measured with a similar observation and retrieval strategy. However, ABI DCOMP shows here a good agreement to MODIS products.

An interesting comparison is the LWP check to AMSR-E data. Note, that only the liquid partition appears in this image, since AMSR-E, as all passive microwave sensors, only measures liquid water. Although the DCOMP product has systematically lower values, the variability in the time series seems to be reliable.

### 2.7.3 Long-period MODIS Analysis

The MODIS microphysical products (MYD06) and MOD06) have proven to be a useful and accurate source of information to the cloud remote sensing community. MODIS is a passive visible and infrared radiometer with a nominal spatial resolution of 1 km at nadir. In this comparison study we use the MODIS algorithm of cloud microphysical properties including cloud optical thickness, liquid and ice water path and cloud droplet effective radius. (Platnick 2003, King 2003)

MODIS level 2 cloud products are derived from a set of channels very similar to those used by DCOMP. Therefore, and in view of potential systematic error sources, comparisons between MODIS retrievals of cloud effective radius, cloud phase and cloud optical depth with corresponding DCOMP products should be performed with caution. Differences to MODIS products are not necessarily a sign of low quality of DCOMP products. It might be a result of the different approaches of the retrievals or the use of different ancillary data, such as the surface albedo, which could cause the differences

To compare the DCOMP results to those from MODIS, we analyzed MODIS data from AQUA and TERRA satellites that was nearly coincident with SEVIRI observations for a full ten days of data (days 230 to 239 in 2006). A 10-day time period provides a high number of matched observations in all possible weather situations. We do not expect a longer time period to show substantially different comparison results. We then compared these results to SEVIRI data that are closest in time. The time threshold is 2 minutes. The spatial threshold is 4 kilometers. We used only pixels in which both datasets have the same phase detected. In this analysis, only pixels where the 0.65  $\mu\text{m}$  values agreed within 12% were used. The rationale for this criterion is that agreement of cloud products is only expected for pixels, which have rough agreement in the observations.

#### 2.7.3.1 Comparison of Cloud Optical Depth

Figure 16 shows comparisons of the Cloud Optical Depth for water and ice with those SEVIRI and MODIS points that met all criteria described above. No additional filtering on the results was applied. The results indicate that the MODIS products were on average 1.59 units higher for water and 1.81 units higher for ice clouds. The corresponding precision values are 4.43 and 5.02 . The agreement is particularly good for thin clouds. The biggest differences appear for water clouds with an cloud optical depth greater than 25. Note that the color bar is logarithmic stretched. The bulk number of matched points is within the depicted specs range.

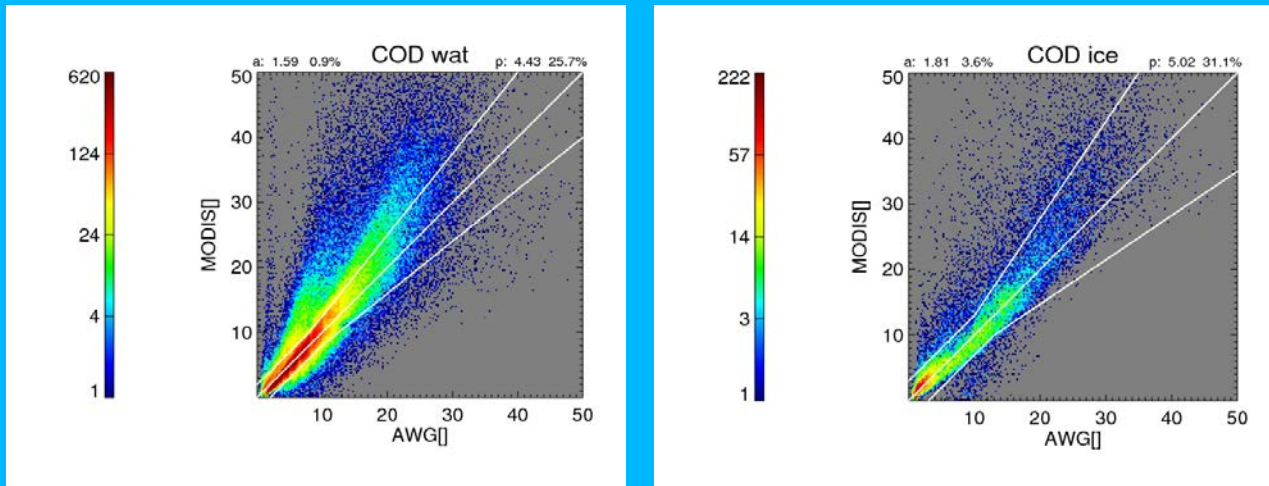


Figure 24 Comparison of Cloud Optical thickness for Days 230-239 in 2006 derived from MODIS (MYD06 and MOD06) products and from DCOMP algorithm. Left image shows results for water phase, right image for ice phase. Accuracy and precision of the comparison are shown in the figures. Specs ranges are added as white lines in the figures.

### 2.7.3.2 Comparison of Cloud Particle Size

Figure 17 shows the same comparison for Cloud Particle Size, referred to here as effective radius (REF). MODIS has mostly bigger values than DCOMP, but the comparison results are within the specs.

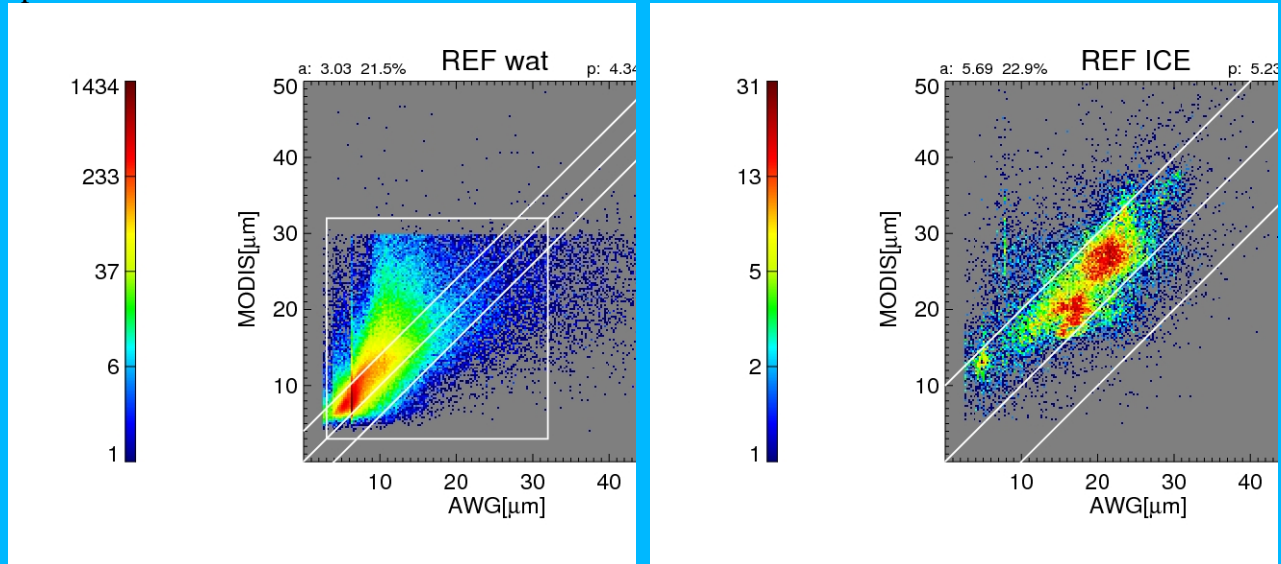


Figure 25 Comparison of Cloud Particle Size for Days 230-239 in 2006 derived from MODIS (MYD06 and MOD06) products and from DCOMP algorithm. Left image shows results for water phase, right image for ice phase. Accuracy and precision of the comparison are shown in the figures. Specs ranges are added as white lines in the figures.

### 2.7.3.3 Comparison of Cloud Optical Depth Ice phase

For both retrievals, the water path is calculated directly from COD and CPS results under certain assumptions of the vertical profile of the cloud particle within the cloud. This approach can lead to bigger differences in a comparison study. Figure 18 shows the results for the 10-day period. For LWP (left side) almost all pixels are in the specs range. However, there is a clear bias for parts of the LWP range. MODIS results show higher values of about 24 percent. The IWP image shows contrary comparison results. DCOMP has much higher values, up to 40 percent higher.

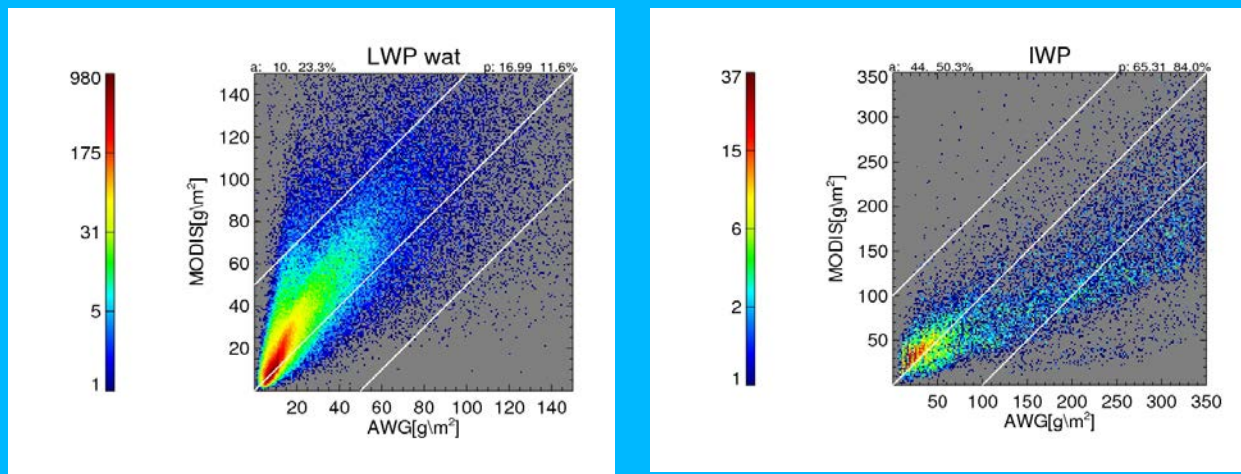


Figure 26 Comparison of Water Path for Days 230-239 in 2006 derived from MODIS (MYD06 and MOD06) products and from DCOMP algorithm. Left image shows results for water phase (LWP), right image for ice phase (IWP). Accuracy and precision of the comparison are shown in the figures. Specs ranges are added as white lines in the figures.

### 2.7.4 Comparison of DCOMP/LWP with AMSR-E

For liquid water path over ocean the passive satellite-based sensor AMSR-E offers a further validation data source. Limitations are different spatial resolution and the exclusive capability over sea and liquid phase. AMSR-E is a passive microwave radiometer onboard NASA's Aqua polar platform. It measures polarized radiances at six frequencies between 6 and 89 GHz.

We follow for this comparison studies from publications by Bennartz 2007, Greenwald 2009 and Juarez 2009. One AMSR-E pixel size is approx. 10x15 km. We use AMSR-E grid as "master" grid to which the "slave" grids of SEVIRI grid is matches. We apply the following matching criteria:

- 90 percent of the field of view of an AMSR-E pixel must be covered by liquid water clouds.
- Since AMSR-E observations are insensitive to thin clouds we exclude observations for COD lower than 5.
- To ensure that we really include only liquid clouds we apply a filter for clouds warmer than 268K.
- We flag out all AMSR-E pixels with a rain flag in quality flag output.

Spatial and temporal matching criteria are 5 kilometers spatial and 5 minutes time difference between the SEVIRI and AMSR-E measurement. For this comparison all SEVIRI pixels over the sea in a grid box with edges at 45E, 65S, 45W and 65N for 5 days in October 2006 and five days in April 2007 were considered.

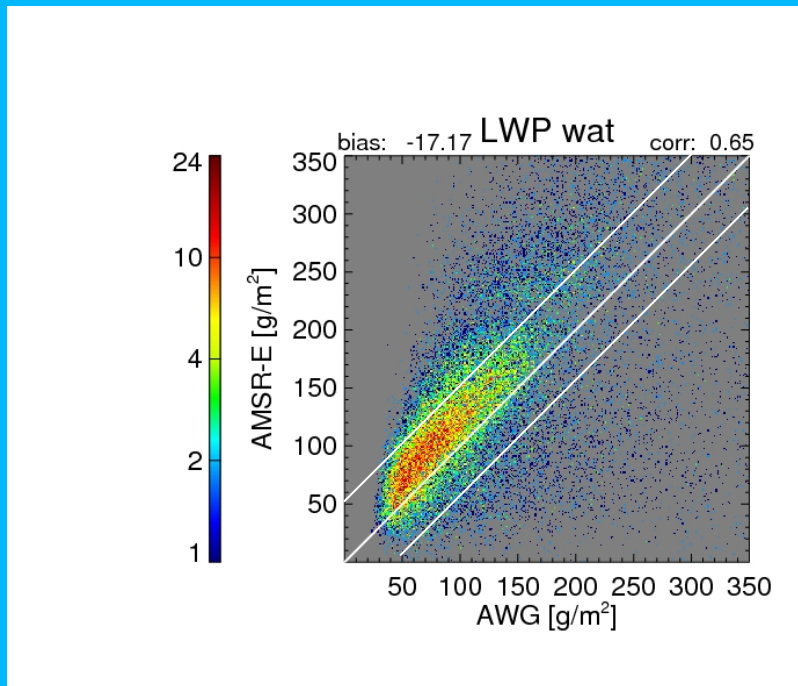


Figure 27 Comparison of AWG-DCOMP Liquid water product to AMSR-E for a two-day period (24-25 August 2006) as a 2D histogram.

Figure 19 shows result for a 10-day period in October 2006 and April 2007. DCOMP (depicted as AWG in Figure 19 ) met the specification of 50 g/m<sup>2</sup> for more than 90 percent of observations.

### 2.7.5 Error Budget

Using the validation described above, the following table provides our estimate of an error budget. DCOMP fulfilled the specifications of accuracy values for all validation data sets. The precision requirements were not met for three of the experiments. This result may be explained as follows:

- The fact that the accuracy meets the specs, but not the precision, may be a result of frequent bad spatial and temporal matches between observations of two different satellites. Even in homogenous cloud regions, the difference can be significant especially for optical depth.
- Calibration between MODIS and SEVIRI channels might be different.
- The atmospheric correction is a function of cloud top pressure. Different CTPs might cause an additional error. A filtering regarding cloud top pressure was not applied.
- Even though the LWP from the AMSR-E observations are the best available and physically reasoned data, the validation remains difficult due to different spatial resolution (5 km vs. 10/15 km).

Table 17 Validation results of DCOMP.

Product	Validation Source	Accuracy	Specs	Precision	Specs
<b>COD Water</b>	MODIS	1.59/0.9%	2. or 20%	4.43/25.7%	2. or 20%
<b>COD Ice</b>	MODIS	1.81/3.6%	3. or 30%	5.02/31.1%	3. or 30%
<b>CPS Water</b>	MODIS	3.03 $\mu$ m	4 $\mu$ m	4.3 $\mu$ m	4 $\mu$ m
<b>CPS Ice</b>	MODIS	5.69 $\mu$ m	10 $\mu$ m	5.23 $\mu$ m	10 $\mu$ m
<b>LWP</b>	MODIS	10g/m <sup>2</sup>	50 g/m <sup>2</sup>	17 g/m <sup>2</sup>	50 g/m <sup>2</sup>
<b>LWP</b>	AMSR-E	17 g/m <sup>2</sup>	50 g/m <sup>2</sup>	47 g/m <sup>2</sup>	50 g/m <sup>2</sup>
<b>IWP</b>	MODIS	44 g/m <sup>2</sup>	100 g/m <sup>2</sup>	65 g/m <sup>2</sup>	100 g/m <sup>2</sup>

### 3 ASSUMPTIONS AND LIMITATIONS

The following sections describe the current limitations and assumptions in the current version of the DCOMP.

#### 3.1 Performance

The following assumptions have been made in developing and estimating the performance of the algorithm. The following list contains the current assumptions and proposed mitigation strategies.

1. NWP data of comparable or superior quality to the current 6 hourly GFS forecasts are available. (Use a default value for water vapor profile over clouds.)
2. Surface albedo values from MODIS are available for each pixel. (Use a default value.)
3. All of the static ancillary data are available at the pixel level. (Reduce the spatial resolution of the surface type, land mask and or coast mask.)
4. The processing system allows for processing of multiple pixels at once for application of the spatial uniformity tests. (No mitigation possible)
5. Channel 2 is available. (No mitigation possible)
6. Channel 6 is available. (No mitigation possible)

#### 3.2 Assumed Sensor Performance

We assume the sensor will meet its current specifications. However, the DCOMP will be dependent on the following instrument characteristics.

- The spatial uniformity tests in the algorithm will be critically dependent on the amount of striping in the data.
- Unknown spectral shifts in some channels will cause biases in the clear-sky RTM calculations that may impact the performance of the algorithm.
- Errors in navigation from image to image will affect the performance of the temporal tests.

### 3.3 Pre-Planned Product Improvements

We have no product improvements planned at the moment.

## 4 REFERENCES

- Bennartz, R. (2007), Global assessment of marine boundary layer cloud droplet number concentration from satellite, *J Geophys Res-Atmos*, 112(D2), -.
- Greenwald (2009), A 2 year comparison of AMSR-E and MODIS cloud liquid water path observations, *Geophysical Research Letters*, 36, L20805, 6 PP., 2009
- Hansen, J. E., and L. D. Travis (1974), Light-Scattering in Planetary Atmospheres, *Space Sci Rev*, 16(4), 527-610.
- Heidinger, A.K.; Foster, M.J.; Walther, A. The pathfinder atmospheres extended (PATMOS-x) AVHRR climate data set. Bull. Am. Meteor. Soc. 2013, doi: 10.1175/BAMS-D-12-00246.1.
- Heymsfield. (2003). Ice Water Path-Optical Relationships for Cirrus and Deep Stratiform Ice Cloud Layers, *J. Appl. Meteor.*, 42(10), 1369-1390.
- Juarez, M., Kahn, B.H., Fetzer, E.J. (2009): Cloud-type dependencies of MODIS and AMSR-E liquid water path differences, *Atmospheric Chemistry and Physics*, 9, 3367-3399
- King, M. D. (1987), Determination of the Scaled Optical-Thickness of Clouds from Reflected Solar-Radiation Measurements, *J Atmos Sci*, 44(13), 1734-1751.
- Mishchenko, M. I., et al. (1996), Sensitivity of cirrus cloud albedo, bidirectional reflectance and optical thickness retrieval accuracy to ice particle shape, *J Geophys Res-Atmos*, 101(D12), 16973-16985.
- Nakajima, T., and M. D. King (1990), Determination of the Optical-Thickness and Effective Particle Radius of Clouds from Reflected Solar-Radiation Measurements .1. Theory, *J Atmos Sci*, 47(15), 1878-1893.
- Nakajima, T., and M. D. King (1992), Asymptotic Theory for Optically Thick Layers - Application to the Discrete Ordinates Method, *Appl Optics*, 31(36), 7669-7683.
- Rodgers, C. D. (2000), *Inverse methods for atmospheric sounding : theory and practice*, xvi, 238 p. pp., World Scientific, Singapore ; [River Edge, N.J.].
- Slingo, A. (1989), A Gcm Parameterization for the Shortwave Radiative Properties of Water Clouds, *J Atmos Sci*, 46(10), 1419-1427.

Stephens, G. L. (1978), Radiation Profiles in Extended Water Clouds .1. Theory, *J Atmos Sci*, 35(11), 2111-2122.

Van de Hulst (1974), Spherical Albedo of a Planet Covered with a Homogeneous Cloud Layer, *Astron Astrophys*, 35(2), 209-214.

Walther, A., Heidinger, AK (2012). Implementation of the Daytime Cloud Optical and Microphysical Properties Algorithm (DCOMP) in PATMOS-x. *JAMC* 51(7), 1371-1390.

Wang, M. H., and M. D. King (1997), Correction of Rayleigh scattering effects in cloud optical thickness retrievals, *J Geophys Res-Atmos*, 102(D22), 25915-25926.

Wiscombe, W. J. (1980), Improved Mie Scattering Algorithms, *Appl Optics*, 19(9), 1505-1509.